SNARE disassembly requires Sec18/NSF side-loading

Yousuf A. Khan[1,2,3,4,9], K. Ian White[1,2,3,4,5], Richard A. Pfuetzner[1,2,3,4,5], Bharti Singal[6], Luis Esquivies[1,2,3,4,5], Garvey Mckenzie[7], Fang Liu[7], Katherine DeLong[1], Ucheor B. Choi[1,2,3,4,5], Elizabeth Montabana[6], Theresa Mclaughlin[7], William T. Wickner[8], Axel T. Brunger[1,2,3,4,5,9]

[1]Department of Molecular and Cellular Physiology, Stanford University, Stanford, CA, USA
[2]Department of Neurology and Neurological Sciences, Stanford University, Stanford, CA, USA
[3]Department of Structural Biology, Stanford University, Stanford, CA, USA
[4]Department of Photon Science, Stanford University, Stanford, CA, USA
[5]Howard Hughes Medical Institute, Stanford University, Stanford, CA, USA
[6]Stanford Cryo-EM microscopy center, Stanford University, Palo Alto, CA, USA
[7]Stanford University Mass Spectrometry, Stanford University, Palo Alto, CA, USA
[8]Department of Biochemistry and Cell Biology, Geisel School of Medicine at Dartmouth, Dartmouth College, Hanover, NH 03755.
[9]Correspondence: yousuf@stanford.edu (YAK), brunger@stanford.edu (ATB)

Abstract

SNARE proteins drive membrane fusion at different cell compartments as their core domains zipper into a parallel four-helix bundle. After fusion, these bundles are disassembled by the AAA+ protein Sec18/NSF and its adaptor Sec17/α-SNAP to make them available for subsequent rounds of membrane fusion. SNARE domains are often flanked by C-terminal transmembrane or N-terminal domains. Previous structures of the NSF–α-SNAP–SNARE complex revealed binding to the D1 ATPase pore, posing a topological constraint as SNARE transmembrane domains would prevent complete substrate threading as suggested for other AAA+ systems. Using mass-spectrometry in yeast cells, we show N-terminal SNARE domain interactions with Sec18, exacerbating this topological issue. We present cryo-EM structures of a yeast SNARE complex, Sec18, and Sec17 in a non-hydrolyzing condition, which show SNARE Sso1 threaded through the D1 and D2 ATPase rings of Sec18, with its folded, N-terminal Habc domain interacting with the D2 ring. This domain does not unfold during Sec18/NSF activity. Cryo-EM structures under hydrolyzing conditions revealed substrate-released and substrate-free states of Sec18 with a coordinated opening in the side of the ATPase rings. Thus, Sec18/NSF operates by substrate side-loading and unloading topologically constrained SNARE substrates.

Main Text

Cellular compartmentalization, growth, hormone secretion, transport, neurotransmission, and many other pathways depend on precise, rapid, and regulated membrane fusion[1,2]. Membrane fusion in eukaryotic cells is mediated by a highly conserved superfamily of SNAREs (Soluble N-ethylmaleimide sensitive factor Attachment protein Receptors)[3]. All SNAREs share a characteristic 60–70 amino acid SNARE domain often flanked by a C-terminal transmembrane domain, membrane anchors, and a folded N-terminal variable domain specific to the SNARE's function and intracellular pathway[4]. SNAREs on opposing membranes interact primarily through their SNARE domains to form a parallel *trans*-SNARE complex, juxtaposing two different membranes[5,6]. Membrane fusion commences when these SNARE domains zipper together in a directed fashion[7,8]. After fusion, the SNAREs form a highly stable parallel helical bundle, the so-called *cis*-SNARE complex[8]. This highly stable four-helix *cis*-SNARE complex is disassembled by Sec18 (N-ethylmaleimide-sensitive factor, NSF, in higher eukaryotes)[9–11] to provide the energy for subsequent membrane fusion events[12].

Sec18/NSF is a universally conserved AAA+ (ATPases associated with diverse cellular activities) protein translocase[13–15]. Sec18/NSF consists of an N-domain, an active D1 AAA+ domain, and a catalytically inactive D2 AAA+ oligomerization domain[16]. It was initially discovered as a critical complementation group required by the yeast secretory pathway, and it is now known for its role in recycling SNAREs[17] and SNARE assembly quality control for proper SNARE complex assembly[18–21]. Sec18/NSF, with the adaptor protein Sec17 (α-SNAP in higher eukaryotes), disassembles *cis*-SNARE complexes. The disassembly requires multiple ATP hydrolysis events in the presence of Mg^{2+}; as few as 6 ATP hydrolysis events are sufficient[22,23].

Cryo-EM structures of the mammalian 20S complex (NSF, α-SNAP, and neuronal SNAREs ternary complex) in a non-hydrolyzing condition (*i.e.*, in the absence of divalent cations) revealed a supramolecular architecture in which the NSF N-domains bind α-SNAP molecules, three or four of which in turn bind the four-helix SNARE complex consisting of the SNARE domains of syntaxin-1A, SNAP-25, and synaptobrevin[10,24]. The N-terminal residues of the SNARE domain of SNAP-25 were bound to the D1 ring pore without apparent ATP hydrolysis, where it interacts with several conserved tyrosine amino acids in a spiral staircase-like pattern[10,13,25]. In these EM maps, no ordered density was observed in the D2 ring pore, consistent with the notion that it is catalytically inactive and primarily responsible for NSF oligomerization rather than substrate engagement[26]. The interaction between the SNARE substrate and the D1 pore is like that observed for other AAA+ translocases and suggests a conserved mechanism for substrate threading through the D1 pore. However, the membrane anchors and domains of the SNAREs would seemingly prevent complete threading of the type suggested for other AAA+ systems[27–29], posing a topological challenge.

Furthermore, SNAREs often contain globular N-terminal domain(s) of variable length and structure; for example, the N-terminal domain of syntaxin consists of a three-helix bundle (Habc domain) involved in regulating its function[30], and the N-terminal domains of Use1 and Sec20 in part form a stable 255 kDa tethering complex[31]. Complete threading would imply that

such N-terminal domains are somehow unfolded. These topological constraints surrounding SNARE loading, processing, and release through Sec18/NSF are further compounded by the observation that Sec18/NSF disassembles all SNAREs in all cellular contexts[3,4,32], which all contain a variety of different N- and C-terminal domains and membrane arrangements/linkages.

In vivo cross-linking mass-spectrometry with Sec18

These questions led us to investigate the space of Sec18/NSF—SNARE interactions through *in vivo* protein crosslinking mass-spectrometry (XL-MS) in yeast. Due to its power as a model system and relatively simple SNARE proteome, *S. cerevisiae* is an excellent model for investigating Sec18 interactions with different substrates in live cells. As such, we developed a protocol for *in vivo* crosslinking mass-spectrometry (XL-MS) in yeast to identify binding partners of Sec18 (**Extended Data Figure 1A, Methods**).

In total, 35 identified proteins are shared between disuccinimidyl glutarate crosslinker (DSG) treated and untreated conditions (*i.e.*, they are non-specific proteins) (**Figure 1A**). The nine proteins observed only in the untreated condition had few unique spectra mapping to their identified proteins, suggesting that they were not detected in the treated condition due to their low abundance and difficulty of consistent detection. The 205 proteins unique to the 5 mM DSG treated condition were processed using spatial analysis of functional enrichment (SAFE) analysis to visualize the various cellular processes to which the identified proteins contribute[33]. At increasing levels of significance thresholds (p = 0.01, 0.001, and 0.0001), the identified proteins only enriched the vesicle trafficking processes. Gene ontology (GO) analysis also revealed lesser-known processes, such as vacuolar acidification and ergosterol biosynthesis (**Supplementary Figure 1**), consistent with Sec18's functions in these contexts[34–36]. The enrichment of these processes validated our crosslinking protocol for specifically targeting Sec18 and its binding partners inside the cell.

Within our enriched protein dataset, we found many yeast SNAREs involved in different pathways and compartments of the cell. We then mapped crosslinked residues of these SNAREs to those of Sec18 (**Figure 1B**). Using a series of empirical constraints (**Methods**), we classified a crosslink as high confidence if it met all constraints, medium confidence if it met some but not all, and low confidence if it did not. Since crosslinking was performed in live cells, we expect these crosslinks to represent interactions between SNAREs and Sec18 during substrate loading, disassembly, and substrate release.

Previous cryo-EM structures of the complex of NSF, α-SNAP, and neuronal SNAREs in a non-hydrolyzing condition revealed that the four-helix SNARE bundle interacts with between two and four α-SNAP molecules, which in turn are bound by the N-domains of NSF; the N-terminal end of one of the SNAREs is bound to the pore of the D1 ring[10,24,25]. Consistent with these structures, we found crosslinks between SNARE domains and the N-domain or D1 domain (examples in **Figure 1C, E, F**). Additionally, we observed several high-confidence crosslinks of yeast SNARE proteins to the D2 domain, an unexpected result given an absence of SNARE density in the D2 ring in these previous cryo-EM structures and that the D2 domain is catalytically inactive[16] and has had no previously reported role in SNARE recycling. Considering

115 this unexpected result, we thus focused on SNAREs with at least one high-confidence crosslink
116 to the D2 domain of Sec18 (**Figures 1C-F**).
117 Specifically, seven of ten high-confidence D2 crosslinks connect to regions N-terminal to
118 a SNARE domain (**Figures 1C-F**). For example, for Sso1, the high-confidence crosslink to D2
119 involves its Habc domain (**Figure 1D, Extended Data Figure 1B**). The Habc domain is a stable
120 three-helix bundle[30]; thus, assuming complete threading through the D1 and D2 pores, the Habc
121 domain (~30 Å diameter) would have to be unfolded transiently. The remaining three high-
122 confidence D2 crosslinks connect to C-terminal regions within SNARE domains. At first glance,
123 this suggests complete substrate threading through both the D1 and D2 rings, akin to other
124 AAA+ protein translocases[37]. However, considering the topology imposed by membrane
125 domains, anchors, and folded N-terminal domains, how is a SNARE substrate loaded and
126 released? To answer these vexing topological questions, we next determined cryo-EM structures
127 of this orthologous yeast complex together with Sec18 and Sec17.
128

129 **The Sec18—Sec17—Sso1—Snc1—Sec9 (y20S) complex**

130 To corroborate the surprising LC-MS/MS results, we determined cryo-EM structures of a
131 yeast SNARE complex together with Sec18 and Sec17. We chose the Sso1—Sec9 —Snc1/Snc2
132 complex (referred to as ySNARE complex) since each component of this complex crosslinked
133 with high confidence to the D2 domain of Sec18 (Snc1 is highly homologous to Snc2). We
134 prepared the Sec18—Sec17—Sso1—Snc1—Sec9 (y20S) complex in a non-hydrolyzing
135 condition (**Extended Data Figure 2, Methods**), and after single particle cryo-EM data collection
136 and processing, we obtained 381,591 high-quality particles that yielded eight 3D classes into
137 which models were built (**Figure 2A–E, Supplementary Figure 2A-B, Supplementary Table**
138 **1**).
139 In the structures of all eight classes, Sso1 is threaded through the D1 pore of Sec18
140 (**Figure 2A**). A characteristic phenylalanine side chain density in Sso1 is present at the same
141 position relative to Sec18 in all classes, allowing for reliable indexing of Sso1. The nucleotide
142 states and the arrangements of D1 around the substrate were also the same among all eight
143 classes, with the ADP-engaged E protomer forming the top of a spiral staircase of tyrosine
144 residues. Protomers D, B, and C were all ATP bound and formed the middle of the staircase. The
145 bottom protomer, A, forms the base of the staircase. Protomer F, with no apparent density for
146 nucleotide in D1, was not associated with Sso1 (**Figure 2B, Extended Data Figure 3A**). This
147 arrangement of the protomers is driven, in part, by the angle between the more mobile D1
148 domain and rigid D2 domain. From protomers E to A, the angle between the D1 and D2
149 decreases monotonically (**Figure 2C**). The protomer at the top of the staircase maintains the
150 largest angle between D1 and D2, while the one at the bottom has the smallest. The eight classes
151 from the non-hydrolyzing y20S dataset also show differences in the ySNARE-Sec17-Sec18-N-
152 domain subcomplex arrangement ("spire") and Sec17 stoichiometry above the D1 ring of the
153 y20S complex before disassembly (**Figure 2D-E, Figure 3A-B**; **Supplementary Discussion**).

The high-confidence crosslinks for Sec18 intra- and inter-protomer interactions are consistent with the cryo-EM structure, specifically with the arrangements of the N-domain and D2-domain (**Figure 3C, Figure 4A**). The high-confidence crosslink between the D1 domain of Sec18 and Snc2 is also consistent with our cryo-EM structures: the D1 domain is proximal to the SNARE domain of Snc2 in the initial loading state of the 20S complex where Sso1 is loaded into the D1 pore. The other high-confidence crosslink occurs between Snc2 and a D2 domain residue at the interface between the D1 and D2 protomers. However, there is no density for Snc2 in our cryo-EM structures in the D1 pore, suggesting that these crosslinks may represent a transient state. Moreover, inter-protomer crosslinks were found between pore loop regions, and between the inter-protomer loop between residues 476 and 490 and N-domain linker regions of D1. These high-confidence crosslinks were within the theoretical maximum crosslinking distance (N_ζ–N_ζ: ~40 Å)[38].

Remarkably, our cryo-EM structures reveal that Sso1 is loaded into both the D1 and the D2 pores since the Habc domain of Sso1 interacts with the outside of the D2 ring, with class 1 having the most well-defined, discrete density (**Figure 4A–E, Extended Data Figure 3B)**. In class 1, the density for Sso1 within Sec18 is continuous from the D1 pore entrance to the D2 pore exit, where the Habc domain begins (**Figure 4A, D**). The three-helix bundle of the Habc domain is then positioned outside the D2 pore, where it packs between two small D2 subdomains (protomers A and B) in an interaction driven by charge complementarity. Indeed, the electrostatic potential surface of the Habc domain forms a roughly opposite that of the bottom of the D2 surface against which it packs (**Figure 4B-C**). Given that this charge distribution is replicated between each pair of D2 subdomains around the D2 surface, it is unsurprising that the Habc domain adopts multiple corresponding rotational states over the eight classes, presumably due to the flexible linker that follows it (**Figure 4E**). This structural observation is consistent with XL-MS data showing a crosslink between the Habc and the D2 domain of Sec18 (**Figure 4A, Extended Data Figure 1B**). Although the putative distance between the crosslinked residues (K570 in Sec18 and K111 of Sso1) observed in the model for class 1 (42 Å) is at the limit for a crosslinking distance, the conformational flexibility of the Habc domain to rotate and exist in multiple conformations about the D2 ring (**Figure 4E**) likely produces conformations well within the crosslinking distance threshold.

Sec18 does not unfold the Sso1/syntaxin Habc domain

Given that this complex was assembled in non-hydrolyzing conditions, we next asked how Sso1 is loaded into Sec18 given the diameter of the Habc domain of Sso1 is ~30 Å, whereas the D1 pore of Sec18 has a diameter of ~11 Å. In other AAA+ translocases like ClpX, ATP hydrolysis drives complete substrate threading through the AAA+ pore[27]. However, in the case of Sec18 in a non-hydrolyzing condition, such complete threading would require the Habc domain to unfold without any energetic input from Sec18.

192 We employed two orthogonal approaches to test if the Sso1 Habc domain unfolds during
193 SNARE disassembly. In our first approach, we used a single-molecule Fluorescence Resonance
194 Energy Transfer (smFRET) system developed previously for NSF, α-SNAP, and neuronal
195 SNAREs[11] in which individual SNARE domains were synthetically linked and stochastically
196 labeled with FRET pairs. This system allows one to observe multiple rounds of SNARE
197 disassembly as the disassembled SNARE domains readily reassemble into a *cis*-SNARE
198 complex due to the covalent linkages. We chose this system since it is well-established.
199 Moreover, it is relevant for the Sec18 system studied here since the primary sequence is
200 conserved in the core regions of Sec18/NSF responsible for ATP hydrolysis and substrate
201 processing (**Extended Data Figure 4A**). In addition, the D1 and D2 rings are structurally
202 conserved when comparing the D1 and D2 rings of Sec18/NSF with engaged substrates, with an
203 average Cα RMSD of 1.64 Å (**Extended Data Figure 4B-C**). The only protomer that exhibits
204 much difference is the F protomer, likely due to its mobility and not due to inherent differences
205 between the structures. Furthermore, we tested the ability of Sec18 and Sec17 to disassemble
206 fluorophore-labeled neuronal SNARE and, *vice versa*, NSF and α-SNAP to disassemble
207 fluorophore-labeled exocytic ySNARE complex (**Extended Data Figure 5A-E, Supplementary**
208 **Discussion**). We found that both could process the species-ortholog SNARE complex, albeit at
209 different rates, further corroborating the interchangeability of NSF and Sec18.
210 We thus used the smFRET assay to study the effect of NSF on the conformation of the
211 three-helix bundle Habc domain of syntaxin during disassembly. We either stochastically labeled
212 the SNARE domains or stochastically labeled the Habc domain at two distinct residue positions
213 to monitor either SNARE disassembly or the folded state of the Habc domain (**Figure 5A**). As in
214 our previous work[11], we observed repeated rounds of disassembly and re-assembly for the
215 SNARE domains as indicated by the changes in single FRET intensity over tens of seconds
216 (**Figure 5B-C**). In stark contrast, we did not observe a change in single-molecule FRET intensity
217 for the labeled Habc domain in non-disassembly and disassembly conditions, producing a FRET
218 intensity distribution consisting only of a high-FRET state (the small peak at 0 is due to traces
219 where acceptor photobleaching occurred since the particular traces never transitioned back to
220 high FRET and no change in the peak intensity between non-disassembly and disassembly
221 conditions was observed) (**Figure 5D-F**). This result suggests that the Habc domain does not
222 unfold during NSF activity.
223 To corroborate this finding with an orthogonal approach for the yeast system, we double-
224 crosslinked the Habc domain of Sso1 by incorporating an unnatural amino acid, 4-azido-L-
225 phenylalanine[39] (**Extended Data Figure 5F-G**). This double crosslink was introduced to prevent
226 the Habc domain from unfolding during any Sec18-driven threading. After crosslinking,
227 confirmed by mass-spectrometry in which we did not detect any uncrosslinked sample
228 (**Extended Data Figure 5G**), we performed a disassembly assay on fluorescently labeled un-
229 crosslinked and crosslinked complexes and monitored progress by native gel electrophoresis
230 (**Figure 5G**). The top band, representing the fully assembled exocytic SNARE complex, is
231 present in both conditions but disappears when adding Mg^{2+} to initiate hydrolysis and the

232 disassembly reaction. There was no qualitative difference in the disassembly between
233 uncrosslinked and crosslinked conditions after normalizing for labeling efficiency (**Figure 5H**).
234 Thus, the folded state of the Habc domain does not change during yeast SNARE disassembly,
235 and crosslinking the Habc domain does not affect the disassembly kinetics. These results for both
236 the yeast and neuronal systems further argue against a threading model of Sso1 engagement
237 since the Habc domain would be unable to pass through the D1 and D2 domains.
238

239 **Substrate-released Sec18 reveals coordinated ring opening**

240 Together, these observations beg the question of how Sso1 enters the Sec18 ATPase
241 rings. To address this topological challenge, we next determined structures of the y20S complex
242 after initiating Sec18 hydrolysis by adding Mg^{2+} (referred to as "hydrolyzing condition").
243 Informed by a fluorescent protein disassembly assay (**Extended Data Figure 5H)**, we initiated
244 the disassembly reaction and waited 7 seconds before sample vitrification.
245 In the resulting cryo-EM dataset, we found a small number of particles (6,356 or 2.26%
246 of final particles, class 1) that consist of entire y20S assemblies (**Figure 6A**), largely similar to
247 those observed in the non-hydrolyzing condition (**Figure 2)**. While the resolution of this
248 reconstruction is low (10.88 Å), the D1 ring is flattened relative to reconstructions from the non-
249 hydrolyzing condition (**Figure 6B**). Considering that our sample consists of purified y20S
250 complexes before initiating disassembly by adding Mg^{2+}, this D1 ring flattening likely occurs
251 due to Mg^{2+} binding or ATP-hydrolysis at one or more subunits.
252 The remaining particles (274,883 or 97.74 % of final particles) were substrate-free
253 (classes 2–4 in **Figure 6C–E**). The D1 ring is also flat in all these substrate-free classes, with all
254 D1 protomers bound to ADP. This uniform binding to ADP, as opposed to the spiral staircase of
255 apo, ADP, and ATP-bound protomers, likely explains the flattened nature of the protomers. In
256 the D2 ring, all protomers are still ATP-bound, consistent with their role in oligomerization.
257 Class 4 consists of a configuration where both the D1 and D2 rings are heptameric (**Figure 6C**),
258 and class 3 is similar to this heptameric class, except the 7th protomer is only partially occupied
259 **(Figure 6D).**
260 Class 2 has a well-resolved hexameric configuration with a coordinated split in class 2 in
261 the D1 and D2 rings (**Figure 6E**). This split spans ~20 Å between protomers and is large enough
262 to accommodate a polypeptide chain entering or leaving the rings. This conformational change is
263 likely induced by the nucleotide state and specifically coupled to the presence of ADP
264 throughout the ring following hydrolysis and SNARE substrate processing. The coordinated split
265 in the D1 and D2 domain rings allows the processed SNARE substrate to be released from the
266 side. This side-release mechanism thus addresses one part of the topological challenge stated
267 above: threading occurs, but the substrate exits from the side, avoiding the membrane domains
268 and linkages in SNARE proteins. We observed similar states, including a coordinate split of the
269 D1 and D2 rings, for the mammalian homolog NSF after processing substrate[25]. This side-release

270 mechanism may also explain the Snc2 crosslink to the residue in the D2 domain that is at the
271 interface between the D1 and D2 protomers (**Figure 1F**).
272

273 **Substrate-free Sec18 reveals coordinated ring opening**

274 Next, we asked if this same side-opening of Sec18 occurs in the hydrolyzing condition without
275 SNARE substrate. We prepared purified wild-type Sec18 in the presence of ATP and Mg^{2+} in a
276 three-stage procedure that yielded a pure sample used for cryo-EM studies (**Extended Data**
277 **Figure 6A-C)**. Two bands were visible in native gels, indicating two oligomeric states
278 (**Extended Data Figure 6D**). Processing and classification led to three classes, two of which
279 appeared to be heptameric and identical (280,935 particles and 73,253 particles, respectively;
280 **Figure 7A**) and the third class, which contained indeterminate density in the D1 ring (70,513
281 particles). Density for the N-domains was not well resolved in any of the classes, presumably
282 due to the conformational flexibility of the N-domains without substrate or adaptor present.

283 3D variability analysis (3DVA)[40] of the third class suggests that it consists of a mixture
284 of heptameric and hexameric Sec18 (**Extended Data Figure 6E),** consistent with the two bands
285 seen on a native gel of the sample**.** The hexameric class reconstructed from 3DVA particle slices
286 from the first mode (**Figure 7B**) is like class 2 observed for the y20S complex under hydrolyzing
287 conditions (**Figure 6E**), wherein hexameric Sec18 has a large, coordinated split in its D1 and D2
288 domain rings without substrate. This similarity in Sec18 conformations provides further evidence
289 that the substrate is both loaded and released through the side of the rings, explaining why the
290 Habc domain is not unfolded during Sec18/NSF activity (**Figure 4**) and that crosslinking the
291 Habc domain does substantially affect the disassembly kinetics (**Figure 5H**). This solves the
292 second part of the topological question posed above.
293 The heptameric class (**Figure 7A**) is nearly identical to class 4 observed in the y20S
294 complex under hydrolyzing conditions (**Figure 6C**). Each protomer in the heptamer is similar to
295 the others, with an average RMSD of <1Å between them, with the angle between the D1 and D2
296 rings varying only with a small range of 61.9°–67.1°, in contrast to hexamer, with a range of
297 60.8°–92.3° (**Figure 2C, Extended Data Figure 6F**). The D1 pore diameter is 30 Å, larger than
298 substrate-bound hexamer, with a diameter of ~11 Å. The substrate-free structures (hexamer and
299 heptamer) are nearly identical (RMSD = 0.48 Å) to the substrate-released structures.
300 To test if these D1 ADP-bound, ring-flattened states of Sec18 observed by single particle
301 cryo-EM convert to a disassembly-competent state, we tested the same protein preparation used
302 for cryo-EM with a vacuolar/lysosome proteoliposome fusion assay[41,42] (**Extended Data Figure**
303 **6H-J, Supplementary Discussion**); this assay confirmed that the Sec18 preparation used for
304 cryo-EM was active and processed vacuolar SNAREs. Moreover, NSF also adopts this flattened
305 ring state and a heptameric or split hexameric arrangement when exchanged into a buffer
306 containing ATP and Mg^{2+} without substrate (**Extended Data Figure 7, Supplementary**

307 **Discussion**) and starting from neuronal 20S complex in a hydrolyzing condition[25], consistent
308 with our observations that Sec18 and NSF share the same functional mechanism.
309
310 **Implications for ATPase activity**
311 The observed structures of Sec18 in substrate-free, substrate-loaded, and substrate-
312 released states suggest large conformational change upon ATP hydrolysis, consistent with
313 previous observations[24,25,43]. In the substrate-free and substrate-released states, examination of
314 the D1 nucleotide binding pockets reveals critical catalytic residues far from the nucleotide
315 (**Figure 7C).** However, in the substrate-engaged state, these conserved residues are tightly bound
316 to nucleotide in a state preceding the binding of divalent cation required to drive hydrolysis.
317 Employing the same statistical workflow used to cluster the different y20S classes (**Methods**),
318 we identified the most significant residues that vary between the no substrate and substrate-
319 bound state by generating an ensemble of models for each class via ensemble refinement
320 (residues colored red in **Figure 7D,** variance contribution per component in **Extended Data**
321 **Figure 5I**). For both the arginine finger loop and Walker B motif, we observed substantial
322 changes to side chain and backbone conformations (**Figure 7E-F**), wherein coordinating residues
323 are positioned closer to the nucleotide-binding pocket in the presence of substrate, presumably
324 establishing a hydrolysis-ready state. In the case of the arginine fingers, the side chain
325 conformational change is likely coupled to nucleotide identity, as hydrolysis disrupts ATP
326 coordination, weakens the interprotomer interface, and leads to rigid body motion of the D1 large
327 subdomain as the arginine fingers disengage. The case of the shift in the Walker B element, on
328 the other hand, appears to be the flexing of the loop without substantial changes to the sidechains
329 of D349 and E350, induced by the motions of pore loop 2 (GVG motif) that bind to the substrate
330 in the pore.
331

332 **Mechanistic details of ring opening**
333 The observed coordinated opening in both the D1 and D2 rings in conditions with and
334 without substrate (**Figures 6 and 7**) suggests a side-release and side-loading mechanism of
335 substrate. We speculate that the conformations of the split Sec18 observed in these multiple
336 conditions are frequently sampled, enabling a substrate to enter or exit the D1-D2 double ring.
337 To better understand the mechanism driving this opening, we compared the flat D1 closed and
338 open conformations of Sec18 (**Figure 6C, E**). The Sec18 protomers are very similar (**Extended**
339 **Data Figures 8A, 8B**), except for the protomers A and F at the split of the D1 and D2 rings.
340 Rigid body motions alter the relative positions of these protomers' respective sub-domains. We
341 performed a conformational analysis to determine which amino acids contributed most to this
342 conformational change between the open and closed states (**Methods**); the eight most significant
343 residues contributing to the variance between the two conformations are shown in **Extended**
344 **Data Figure 8C**. These residues are located in flexible regions between the structured sub-
345 domains of a protomer (**Extended Data Figure 8D)**, where changes to the backbone ϕ and ψ

346 angles of these residues lead to rigid body motions of subdomains. For example, four of the eight
347 residues (R409, F410, L418, N690) are in the linker region between the large and small
348 subdomains of the D1 domain, while G514 is situated between the D1 and D2 domains. These
349 small and large subdomain movements, along with relative motion between the D1 and D2
350 domains, lead to the split that allows substrate loading or release. Given that this opening is
351 hydrolysis independent and occurs regardless of the presence of substrate, it is likely that Sec18
352 samples these states upon thermal agitation; subsequently, substrate enters the pore and locks the
353 D1 and D2 rings into an active hexameric form (*i.e.*, the 20S/y20S complex), possibly in concert
354 with N-domain engagement.
355

356 **Discussion**

357 Based on our LC-MS/MS, structural, and functional results, we propose the following
358 model for SNARE recycling (**Figure 7G**), consisting of four phases. Sec18/NSF transiently
359 forms split-open conformation of both D1 and D2 domain rings in the resting phase with no
360 substrate. Once the *cis*-SNARE complex has been coated with adaptor Sec17/α-SNAP
361 molecules, the Sec18 N-domains can bind the subcomplex and position the unstructured linker
362 connecting the N-terminal Sso1 Habc domain to the SNARE domain proximal to the D1/D2 split
363 without unfolding of the Sso1 Habc domain (**Figure 5H**), thus promoting the loading of
364 substrate into the catalytic core of the enzyme. More generally, this side-loading mechanism
365 would allow Sec18/NSF to process complexes incorporating all SNAREs in the cell regardless of
366 the presence of folded N-terminal domains, provided that, in the latter case, a long enough linker
367 connects them to the following SNARE domain. Upon forming the (y)20S complex, ATP-driven
368 hydrolysis likely fuels the disassembly of the (y)SNARE complex by some degree of threading,
369 accompanied by D1 ring flattening. In the case of Sso1, since full threading cannot occur due to
370 the transmembrane domain, partial melting of the N-terminal end of the SNARE domain could
371 be sufficient to destabilize the SNARE complex. Finally, the pore-bound SNARE is released
372 through the side-split of both the D1 and D2 rings, regardless of membrane anchors or
373 transmembrane domains in SNARE proteins. We observed a similar coordinated opening of the
374 D1 and D2 rings for the mammalian homolog NSF after processing substrate[25]. The syntaxin
375 Habc domain also does not unfold during NSF/mediated disassembly of the ternary SNARE
376 complex (**Figure 5A-G**). The side-loading/release mechanism explains how Sec18/NSF can
377 disassemble SNAREs with constrained topologies.
378 As observed in our cross-linking LC-MS/MS experiments (**Figure 1**), the Sec18 D2 ring
379 can interact not just with the Habc domain of Sso1 but also with other N-terminal accessory
380 domains (such as GOS1, TLG1, and TLG2). In turn, N-terminal domains of SNAREs often
381 interact with other factors. For example, the trimeric Dsl1 complex binds to the SNAREs Use1,
382 Ufe1, and Sec20 through interactions with N-terminal SNARE domains. This 255 kDa complex
383 tethers endoplasmic reticulum membranes together before forming the *trans*-SNARE complex
384 and likely remains complexed before, during, and after fusion[31]. Another example is HOPS, a

385 hexameric complex that tethers lysosomal/vacuolar membranes and orchestrates their fusion[44].
386 HOPS has two Rab-binding subunits for tethering and a SNARE binding subunit that catalyzes
387 initial SNARE complex assembly[45]. Sec18/NSF and Sec17/α-SNAP cooperate with HOPS to
388 ensure rapid and efficient SNARE-mediated fusion[46,47]. For the case of Dsl1, the N-terminal
389 domains of SNAREs remain in a supramolecular arrangement that must be bypassed. For
390 vacuolar/lysosomal fusion, SNAREs must be preprocessed and handed off to the HOPS
391 complex. These complexes impose topological constraints on both ends of the SNAREs that can
392 be resolved by side-loading and side-release.
393 We observed heptameric states of Sec18 (**Figure 6C**) and NSF (**Extended Data Figure**
394 **7A**), split-open hexameric states of Sec18 (**Figure 6E**) and NSF[25] , and a transition between
395 split-hexamer and heptamer of Sec18 (**Figure 6D**). Hydrolysis likely accelerates the transition
396 from hexameric to heptameric state via the split-open state for two related reasons. First, while
397 ring splitting itself is hydrolysis-independent, hydrolysis is associated with large-scale
398 conformational change in the ATPase rings and likely increases the frequency of sampling the
399 open state. Second, we have not observed the heptamer in a substrate-engaged state. Moreover, it
400 seems unlikely that a heptamer could accommodate substrate given the changes heptamerization
401 induces in the N- and D1- layers of the oligomer (an increased diameter would interfere with
402 SNAP recognition of substrate and substrate engagement in the pore). As such, it seems
403 reasonable that heptamer is enriched under hydrolyzing conditions either in the absence of
404 SNARE substrate or in which a significant fraction of SNARE complexes have been
405 disassembled—the hexamer samples the open state and the seventh protomer enters in the
406 absence of SNARE substrate. Thus, the heptameric state, which is unable to process substrate,
407 may not occur in the cell, as there is likely an abundance of *cis*-SNARE substrate and ATP to
408 capture. Moreover, the XL-MS data cannot disentangle the presence of a hexamer or heptamer
409 due to the small overall changes in residue distances between states. We conclude that
410 NSF/Sec18 is mostly hexameric in the cell unless there is a significant dearth of substrate to
411 process.
412 How broadly applicable is this AAA+ side-loading/release mechanism beyond
413 NSF/Sec18? The NSF/Sec18 protein family is highly related to the p97/cdc48 family; both are
414 clade 3 AAA+ machines with two AAA+ rings[13]. For p97/cdc48, their substrate is a
415 polyubiquitinated molecule, again imposing topological restraints. In cryo-EM structures of
416 cdc48 with substrate in non-hydrolyzing conditions, the substrate is threaded through the D1 and
417 D2 rings, presumably without any ATP hydrolysis[48]. This study also showed that distal ubiquitin
418 molecules on a substrate do not unfold during cdc48 activity. These observations suggest that
419 this side-load and side-release mechanism may be employed by cdc48/p97 as well. Lastly, a split
420 p97 structure was observed when bound to a cofactor[49]. This p97 structure also displayed a
421 coordinated split in its D1 and D2 rings with flattened conformations, similar to those observed
422 for Sec18, suggesting a conserved mechanism.
423 Finally, we note that distantly related AAA+ clamp loaders and their clamp also load
424 their nucleic acid substrate from the side[50]. DNA is loaded into an open clamp and AAA+ clamp

loader. Once the clamp loader recognizes the substrate, the ATPase is triggered, and the clamp loader closes the complex around the DNA. Once the clamp is fully secured, the clamp-loader is then released. This shared mechanism suggests the possibility of side-loading and release across the entire AAA+ protein family.

Acknowledgments

We thank the late William I. Weis and Joseph D. Puglisi for stimulating discussions. We thank the National Institutes of Mental Health (NIMH) for support (RO1MH63105 to A.T.B., 1F31MH134477 to Y.A.K.). Y.A.K was additionally supported in part by an NSF GRFP and the Knight-Hennessy Scholarship. K.I.W. was supported by a postdoctoral fellowship from the Helen Hay Whitney Foundation, supported by the Howard Hughes Medical Institute. W.T.W. is supported by a grant from the NIH (2R35GM118037). We thank the Vincent Coates Foundation Mass Spectrometry Laboratory, Stanford University Mass Spectrometry (RRID:SCR_017801) for utilizing the Thermo Orbitrap Eclipse nanoLC/MS system (RRID:SCR_022212) that was purchased with funding from the National Institutes of Health Shared Instrumentation Grant 1S10OD030473, the Stanford Cancer Institute Proteomics/Mass Spectrometry Shared Resource (NIH P30 CA124435). This article is subject to HHMI's Open Access to Publications policy. HHMI laboratory heads have previously granted a non-exclusive CC BY 4.0 license to the public and a sublicensable license to HHMI in their research articles. Pursuant to those licenses, the author-accepted manuscript of this article can be made freely available under a CC BY 4.0 license immediately upon publication.

Author contributions

Y.A.K and A.T.B conceived and designed experiments. K.I.W, B.S., and E.M. assisted Y.A.K. with cryo-EM data collection. Y.A.K. performed and analyzed all experimental data. K.I.W. assisted Y.A.K. with cryo-EM data processing and model building. R.A.F. and L.E. assisted with protein purification. G.M., F.L., and T.M. assisted with high-resolution MS proteomics data collection and analysis. K.D. assisted with bulk disassembly assays. U.B.C. collected and assisted with smFRET data. W.T.W. performed and analyzed vacuolar fusion assays. Y.A.K., A.T.B., and K.I.W. wrote the manuscript.

Competing Interest Statement:

All authors declare no competing interests.

459 **Figure Legends**

460 **Figure 1: *In vivo* crosslinking mass-spectrometry of Sec18**
461 **a,** Top left: Venn diagram of proteins found in the condition without a crosslinking agent (red)
462 added and with crosslinking agent added (green). Bottom right: SAFE-analysis[33] of yeast
463 proteins that specifically crosslink to Sec18. Blobs represent enrichments in the pathway. Blobs
464 of different colors represent enrichments that are specific to different p-value thresholds (brown
465 < 0.01, blue < 0.001, red < 0.0001. p-values are derived from Fisher's exact test with Bonferroni
466 correction for multiple testing). **b,** Heatmap of yeast SNARE proteins crosslinking to specific
467 Sec18 positions. The Sec18 primary sequence along the x-axis is colored coded by domain, and
468 yeast SNARE proteins with at least one medium confidence crosslink are shown along the y-
469 axis. Red squares represent positions where one or more manually verified, high-confidence
470 crosslinks were found (**Methods**). Orange squares represent where one or more manually
471 verified medium-confidence crosslinks were found. White squares represent positions in which
472 manually verified crosslinks were not found or were of low confidence. **c-f,** Crosslinking
473 schematic of Sec18 and SNAREs that contain at least one high-confidence crosslink to the Sec18
474 D2 domain. Red dashed lines represent high-confidence crosslinks, and orange dashed lines
475 represent medium-confidence crosslinks.
476

477 **Figure 2: The y20S supramolecular complex**
478 **a,** Domain diagrams of the components used to prepare the y20S complex; coloring follows this
479 throughout (top left). The structure of class 1 of y20S, with ATP and ADP nucleotides (red and
480 blue, respectively; bottom right). Cryo-EM density for class 1 and the Sso1 atomic model around
481 residue F173 (inset, bottom left). **b,** Sso1 substrate is engaged by Y315 in all D1 protomers with
482 bound nucleotide. **c,** Conformations of the protomers of Sec18 when engaged to substrate. **d**,
483 Top-down views of class 1 and class 8 cryo-EM maps. **e,** Cartoon top-down views of eight y20S
484 classes. These classes differ primarily by spire configuration, *i.e.*, the pattern of N-domain and α-
485 SNAP engagement.
486

487 **Figure 3: Intra and inter-protomer crosslinks mapped on the y20S complex structure**
488 **a,** Electrostatic surface potentials of the interaction between SNAREs and Sec17. Negatively
489 charged regions are colored red, and positive ones are colored blue. **b,** Electrostatic surface
490 potentials of the interaction between Sec17 and the N-domains of Sec18. Alternating views of
491 these interactions are shown to demonstrate the complementarity of the electrostatic interactions.
492 **c,** For clarity, only two Sec18 protomers of the y20S complex are shown. The black dashed lines
493 represent crosslinks designated as high quality and superimposed over the diagram. The two
494 insets show close-up views of two inter-protomer crosslinks.
495

496 **Figure 4: Sso1 is threaded through the D1 and D2 domains**
497 **a,** y20S class 1 atomic model emphasizing the position of Sso1. Stars represent the crosslink
498 identified by crosslinking mass spectrometry (**Figure 1B**). **b,** Bottom view of y20S class 1 D1

499 ring; the Habc domain is packed against the D2 ring surface, between protrusions corresponding
500 to the C-terminal helical regions of two D2 small subdomains. All surfaces are colored grey,
501 except for protomers A and B, which are colored by their electrostatic potential **c,** Rotated view
502 of y20S class 1 relative to **b** showing the Habc tucked between protomers A and B with now the
503 Habc domain colored by its electrostatic potential **d,** Composite cryo-EM map (blue, Relion-
504 unsharpened map: Habc domain and D1 density and CryoSPARC 3DFlex map: D2 density) of
505 y20S class 1. **e,** Cryo-EM maps of all eight y20S classes reveal the Habc domain associated with
506 the Sec18 D2 ring in all classes (red). In 6/8 classes, the Habc density is radially averaged into
507 multiple discrete positions around the D2 ring, leading to more diffuse density.
508
509 **Figure 5: Sec18/NSF does not unfold the Habc domain**
510 **a,** Diagram of the smFRET disassembly/re-assembly assay with NSF/α-SNAP and linked
511 neuronal SNAREs. Either the linked SNAREs complex is stochastically labeled (residue number
512 249 in syntaxin and residue number 82 in synaptobrevin) or the syntaxin Habc domain is
513 stochastically labeled (residue numbers 35 and 105 in the Habc domain). **b,** Representative traces
514 of labeled linked SNARE complex in the non-hydrolyzing condition. Green represents the
515 acceptor, and red represents the donor-dye fluorescence-intensity time traces. n = 53. **c,**
516 Representative time trace of labeled SNARE complex in disassembly conditions, the black line
517 represents fitting by a vbGMM[51]. n = 114. **d,** Representative time-trace of labeled Habc domain
518 in the non-hydrolyzing condition. Green represents the donor, and red is the acceptor dye
519 fluorescence intensity time-traces. n = 27. **e,** Representative time-trace of labeled Habc domain
520 in disassembly conditions. The black line represents fitting a vbGMM. n = 22. **f,** Histograms of
521 E-FRET for all four conditions. The blue dotted line represents a Gaussian fit of the data. The y-
522 axis is the normalized frequency of occurrence of the E-FRET states in the traces. Top left:
523 SNARE E-FRET for the non-hydrolyzing condition, top right: SNARE E-FRET for the
524 hydrolyzing condition. Habc E-FRET for the non-hydrolyzing condition (bottom left). Habc E-
525 FRET for the hydrolyzing condition (bottom right). **g,** Native gel of labeled uncrosslinked or
526 crosslinked yeast SNARE complex that has been labeled with Oregon Green Maleimide 488. **h,**
527 Quantification of gel densitometry of n = 3 independent disassembly experiments. Error bars
528 represent the standard deviation of the mean. Densitometries were all normalized to 0 min
529 values.
530
531 **Figure 6: Post-disassembly of y20S reveals substrate-released states**
532 **a,** Cryo-EM map of y20S in the hydrolyzing condition, colored by domain. **b**, The distance
533 between the D1 and D2 domains decreases for some protomers under hydrolyzing conditions,
534 leading to D1 ring flattening. The orange model corresponds to protomer E from the merged
535 D1/D2 focused class in the non-hydrolyzing condition, which was rigid-body fit into the density
536 of the hydrolyzing condition to generate the blue model. **c,** Cryo-EM map and model of class 4
537 of Sec18, showing a heptamer. **d,** Cryo-EM map and atomic model of class 3 of Sec18,
538 suggesting a transition state. **e, Cryo-**EM map and atomic model of class 2 of Sec18, showing a

split hexamer. In panels **c-e**, the top is the EM-map, while the middle and bottom show atomic models in top and side views, respectively.

Figure 7: Structures of substrate-free Sec18 in the hydrolyzing condition

a, Atomic model of the substrate-free heptameric state of Sec18 (class 1). **b,** Atomic model of the split substrate-free hexameric state of Sec18 (derived from 3DVA of class 3). **c,** The D1 nucleotide binding pocket is remodeled as a function of SNARE substrate binding and nucleotide state. The arginine fingers R406 and R409 are contributed by the neighboring protomer. The substrate-free and substrate-released states are nearly identical in conformation. Water molecules are shown as red spheres. **d**, Atomic model of Sec18 with protomer A colored blue if not a significant residue from conformational analysis and colored red if significant (p-value < 0.05). **e,** Atomic models show the difference of the arginine finger loop in the no substrate (transparent) and substrate condition. **f,** Atomic models of the loop proximal to the Walker B motif in the no substrate (transparent) and substrate condition. For **d-f**, residues are colored red if they are in the top 5% of residues that significantly vary between conditions. **g.** We propose a general model of SNARE recycling, regardless of the cellular context. First, a *cis*-SNARE complex is coated with at least 1 Sec17/α-SNAP adaptor molecule, allowing Sec18/NSF to recognize it. The SNARE substrate is then loaded into a split hexamer with a coordinated opening in both D1 and D2 rings through the side, bypassing whatever N-terminal domains may be present. The substrate is then threaded coaxially through the Sec18/NSF pore. Upon completion of processing, the SNARE substrate is released through the side, bypassing the topological constraints of the membrane. Finally, Sec18 returns to its 'resting' state until more substrate is encountered. Yellow arrows indicate the direction of loading and release.

References

1. Wickner, W. & Schekman, R. Membrane fusion. *Nat. Struct. Mol. Biol.* **15**, 658–664 (2008).
2. Südhof, T. C. Neurotransmitter Release: The Last Millisecond in the Life of a Synaptic Vesicle. *Neuron* **80**, 675–690 (2013).
3. Jahn, R., Cafiso, D. C. & Tamm, L. K. Mechanisms of SNARE proteins in membrane fusion. *Nat. Rev. Mol. Cell Biol.* 1–18 (2023) doi:10.1038/s41580-023-00668-x.
4. Ungar, D. & Hughson, F. M. SNARE Protein Structure and Function. *Annu. Rev. Cell Dev. Biol.* **19**, 493–517 (2003).
5. Rizo, J. Molecular Mechanisms Underlying Neurotransmitter Release. *Annu. Rev. Biophys.* **51**, 377–408 (2022).

574 6. Liang, B., Kiessling, V. & Tamm, L. K. Prefusion structure of syntaxin-1A suggests pathway
575 for folding into neuronal trans-SNARE complex fusion intermediate. *Proc. Natl. Acad. Sci.*
576 **110**, 19384–19389 (2013).
577 7. Weber, T. *et al.* SNAREpins: Minimal Machinery for Membrane Fusion. *Cell* **92**, 759–772
578 (1998).
579 8. Sutton, R. B., Fasshauer, D., Jahn, R. & Brunger, A. T. Crystal structure of a SNARE
580 complex involved in synaptic exocytosis at 2.4 Å resolution. *Nature* **395**, 347–353 (1998).
581 9. Söllner, T., Bennett, M. K., Whiteheart, S. W., Scheller, R. H. & Rothman, J. E. A protein
582 assembly-disassembly pathway in vitro that may correspond to sequential steps of synaptic
583 vesicle docking, activation, and fusion. *Cell* **75**, 409–418 (1993).
584 10. White, K. I., Zhao, M., Choi, U. B., Pfuetzner, R. A. & Brunger, A. T. Structural principles
585 of SNARE complex recognition by the AAA+ protein NSF. *eLife* **7**, e38888 (2018).
586 11. Choi, U. B. *et al.* NSF-mediated disassembly of on- and off-pathway SNARE complexes and
587 inhibition by complexin. *eLife* **7**, e36497 (2018).
588 12. Yoon, T.-Y. & Munson, M. SNARE complex assembly and disassembly. *Curr. Biol.* **28**,
589 R397–R401 (2018).
590 13. Khan, Y. A., White, K. I. & Brunger, A. T. The AAA+ superfamily: a review of the
591 structural and mechanistic principles of these molecular machines. *Crit. Rev. Biochem. Mol.*
592 *Biol.* **57**, 156–187 (2022).
593 14. Hanson, P. I. & Whiteheart, S. W. AAA+ proteins: have engine, will work. *Nat. Rev. Mol.*
594 *Cell Biol.* **6**, 519–529 (2005).

595 15. Puchades, C., Sandate, C. R. & Lander, G. C. The molecular principles governing the
596 activity and functional diversity of AAA+ proteins. *Nat. Rev. Mol. Cell Biol.* **21**, 43–58
597 (2020).
598 16. Nagiec, E. E., Bernstein, A. & Whiteheart, S. W. Each Domain of the N-Ethylmaleimide-
599 sensitive Fusion Protein Contributes to Its Transport Activity (*). *J. Biol. Chem.* **270**, 29182–
600 29188 (1995).
601 17. Novick, P., Field, C. & Schekman, R. Identification of 23 complementation groups required
602 for post-translational events in the yeast secretory pathway. *Cell* **21**, 205–215 (1980).
603 18. Ma, C., Su, L., Seven, A. B., Xu, Y. & Rizo, J. Reconstitution of the vital functions of
604 Munc18 and Munc13 in neurotransmitter release. *Science* **339**, 421–425 (2013).
605 19. Lai, Y. *et al.* Molecular Mechanisms of Synaptic Vesicle Priming by Munc13 and Munc18.
606 *Neuron* **95**, 591-607.e10 (2017).
607 20. Gao, Y. *et al.* Sensory deficit screen identifies nsf mutation that differentially affects SNARE
608 recycling and quality control. *Cell Rep.* **42**, 112345 (2023).
609 21. Leitz, J. *et al.* Beyond the MUN domain, Munc13 controls priming and depriming of
610 synaptic vesicles. *Cell Rep.* **43**, 114026 (2024).
611 22. Ryu, J.-K. *et al.* Spring-loaded unraveling of a single SNARE complex by NSF in one round
612 of ATP turnover. *Science* **347**, 1485–1489 (2015).
613 23. Ryu, J.-K., Jahn, R. & Yoon, T.-Y. Review: Progresses in understanding N-ethylmaleimide
614 sensitive factor (NSF) mediated disassembly of SNARE complexes. *Biopolymers* **105**, 518–
615 531 (2016).
616 24. Zhao, M. *et al.* Mechanistic insights into the recycling machine of the SNARE complex.
617 *Nature* **518**, 61–67 (2015).

618 25. White, K. I. *et al.* NSF converts syntaxin clusters to a priming-ready state. *Unpublished*.
619 26. Whiteheart, S. W. *et al.* N-ethylmaleimide-sensitive fusion protein: a trimeric ATPase whose
620 hydrolysis of ATP is required for membrane fusion. *J. Cell Biol.* **126**, 945–954 (1994).
621 27. Maillard, R. A. *et al.* ClpX(P) Generates Mechanical Force to Unfold and Translocate Its
622 Protein Substrates. *Cell* **145**, 459–469 (2011).
623 28. de la Peña, A. H., Goodall, E. A., Gates, S. N., Lander, G. C. & Martin, A. Substrate-
624 engaged 26S proteasome structures reveal mechanisms for ATP-hydrolysis–driven
625 translocation. *Science* **362**, eaav0725 (2018).
626 29. Rizo, A. N. *et al.* Structural basis for substrate gripping and translocation by the ClpB AAA+
627 disaggregase. *Nat. Commun.* **10**, 2393 (2019).
628 30. Fernandez, I. *et al.* Three-dimensional structure of an evolutionarily conserved N-terminal
629 domain of syntaxin 1A. *Cell* **94**, 841–849 (1998).
630 31. DAmico, K. A. *et al.* Structure of a membrane tethering complex incorporating multiple
631 SNAREs. *Nat. Struct. Mol. Biol.* 1–9 (2024) doi:10.1038/s41594-023-01164-8.
632 32. Wang, T., Li, L. & Hong, W. SNARE proteins in membrane trafficking. *Traffic* **18**, 767–775
633 (2017).
634 33. Baryshnikova, A. Systematic Functional Annotation and Visualization of Biological
635 Networks. *Cell Syst.* **2**, 412–421 (2016).
636 34. Thomas, P. D. *et al.* PANTHER: Making genome-scale phylogenetics accessible to all.
637 *Protein Sci.* **31**, 8–22 (2022).
638 35. Kato, M. & Wickner, W. Ergosterol is required for the Sec18/ATP-dependent priming step
639 of homotypic vacuole fusion. *EMBO J.* **20**, 4035–4040 (2001).

640 36. Ungermann, C., Wickner, W. & Xu, Z. Vacuole acidification is required for trans-SNARE
641 pairing, LMA1 release, and homotypic fusion. *Proc. Natl. Acad. Sci.* **96**, 11194–11199
642 (1999).
643 37. Baker, T. A. & Sauer, R. T. ClpXP, an ATP-powered unfolding and protein-degradation
644 machine. *Biochim. Biophys. Acta BBA - Mol. Cell Res.* **1823**, 15–28 (2012).
645 38. Merkley, E. D. *et al.* Distance restraints from crosslinking mass spectrometry: Mining a
646 molecular dynamics simulation database to evaluate lysine–lysine distances. *Protein Sci.*
647 *Publ. Protein Soc.* **23**, 747–759 (2014).
648 39. Chin, J. W. *et al.* Addition of p-Azido-l-phenylalanine to the Genetic Code of Escherichia
649 coli. *J. Am. Chem. Soc.* **124**, 9026–9027 (2002).
650 40. Punjani, A. & Fleet, D. J. 3D variability analysis: Resolving continuous flexibility and
651 discrete heterogeneity from single particle cryo-EM. *J. Struct. Biol.* **213**, 107702 (2021).
652 41. Zucchi, P. C. & Zick, M. Membrane fusion catalyzed by a Rab, SNAREs, and SNARE
653 chaperones is accompanied by enhanced permeability to small molecules and by lysis. *Mol.*
654 *Biol. Cell* **22**, 4635–4646 (2011).
655 42. Zick, M., Stroupe, C., Orr, A., Douville, D. & Wickner, W. T. Membranes linked by trans-
656 SNARE complexes require lipids prone to non-bilayer structure for progression to fusion.
657 *eLife* **3**, e01879.
658 43. Shein, M. *et al.* Characterizing ATP processing by the AAA+ protein p97 at the atomic level.
659 *Nat. Chem.* **16**, 363–372 (2024).
660 44. Shvarev, D. *et al.* Structure of the HOPS tethering complex, a lysosomal membrane fusion
661 machinery. *eLife* **11**, e80901 (2022).

662 45. Song, H., Orr, A. S., Lee, M., Harner, M. E. & Wickner, W. T. HOPS recognizes each
663 SNARE, assembling ternary trans-complexes for rapid fusion upon engagement with the 4th
664 SNARE. *eLife* **9**, e53559 (2020).
665 46. Song, H., Torng, T. L., Orr, A. S., Brunger, A. T. & Wickner, W. T. Sec17/Sec18 can
666 support membrane fusion without help from completion of SNARE zippering. *eLife*
667 https://elifesciences.org/articles/67578 (2021) doi:10.7554/eLife.67578.
668 47. Orr, A. & Wickner, W. Sec18 supports membrane fusion by promoting Sec17 membrane
669 association. *Mol. Biol. Cell* **33**, ar127 (2022).
670 48. Twomey, E. C. *et al.* Substrate processing by the Cdc48 ATPase complex is initiated by
671 ubiquitin unfolding. *Science* **365**, eaax1033 (2019).
672 49. Braxton, J. R. *et al.* The p97/VCP adaptor UBXD1 drives AAA+ remodeling and ring
673 opening through multi-domain tethered interactions. *Nat. Struct. Mol. Biol.* **30**, 2009–2019
674 (2023).
675 50. Kelch, B. A., Makino, D. L., O'Donnell, M. & Kuriyan, J. Clamp loader ATPases and the
676 evolution of DNA replication machinery. *BMC Biol.* **10**, 34 (2012).
677 51. Verma, A. R., Ray, K. K., Bodick, M., Kinz-Thompson, C. D. & Gonzalez, R. L. Increasing
678 the accuracy of single-molecule data analysis using tMAVEN. *Biophys. J.* (2024)
679 doi:10.1016/j.bpj.2024.01.022.
680

681 **Methods**

682 **HA-Sec18 *S. cerevisiae* strain preparation and treatment**

683 Briefly, we created an *S. cerevisiae* strain containing HA-tagged Sec18 and treated it with
684 zymolyase and lyticase to dissolve its cell wall but maintain its integrity as a living cell
685 (spheroplast). We then incubated the spheroplasts with disuccinimidyl glutarate (DSG), a
686 membrane permeable protein crosslinking agent, for 30 minutes before cellular lysis and anti-HA

687 co-immunoprecipitation (coIP) to isolate Sec18 and any bound proteins to it. This sample was
688 then subjected to SDS-PAGE gel electrophoresis, and the bands corresponding to crosslinked
689 Sec18 were excised and sent for liquid chromatography-mass spectrometry (LC-MS/MS)
690 analysis. More specifically, tagged Sec18 (pYK175, 3x-Flag N-terminal, HA-tag C-terminal)
691 plasmid was transformed into *S. cerevisiae* S288C using the Frozen-EZ Yeast Transformation
692 Kit (Zymo Research T2001). Expression of tagged Sec18 was accomplished by growing yeast in
693 1% raffinose and 1% galactose media. Cells were spun down and treated with 100 units of
694 zymolyase (Zymo Research #1004) at 37°C for 1 hour. After incubation, spheroplasts were
695 pelleted with a 1000 xg spin. DSG diluted in 1x PBS was used to resuspend the pellet, and the
696 sample was incubated for 30 minutes. The excess DSG was then quenched with 1M Tris and
697 incubated for another 15 minutes. Cells were washed with cold PBS and were resuspended in
698 lysis buffer (5mM EDTA, 1mM ATP, 1mM TCEP, 150 mM NaCl, 10% glycerol, 0.5% NP40,
699 and 50 mM HEPES pH 7.4) and glass beads (BioSpec 11079105). This bead-lysis-cell solution
700 was vortexed for 5 minutes at 4°C three times with ice incubations between each vortexing. The
701 solution was then spun down at 10,000 xg for 5 minutes at 4°C. The supernatant was taken and
702 then spun down again at 10,000 xg for 15 minutes at 4°C. The supernatant was then taken and
703 subjected to magnetic-bead anti-HA coIP (Thermo Scientific 88838). The eluant of the beads
704 was run on an SDS-PAGE gel, and the bands corresponding to Sec18 were excised.
705
706
707 **XL-MS sample preparation**
708 Protein samples were embedded in Coomassie-stained gel bands, fixed in 1% acetic acid.
709 The gels were washed several times in 50 mM ammonium bicarbonate, followed by reduction
710 with 10 mM of dithriothreitol (DTT) and incubation for twenty minutes at room temperature.
711 They were then alkylated using 30 mM acrylamide for 30 minutes. This was proceeded by
712 overnight digestion at 37 degrees Celsius with 500ng of mass spectrometry grade trypsin/LysC
713 mix (Promega). Post-digestion, samples were quenched with formic acid (adjusted to a pH ~3)
714 and desalted using MonoSpin C18 Solid-Phase Extraction (SPE) columns (GL Sciences).
715 Finally, the samples were dried via SpeedVac (Thermo Scientific, San Jose, CA) and exchanged
716 into LC-MS reconstitution buffer (2% acetonitrile with 0.1% formic acid in water) for
717 instrumental analysis.
718
719
720 **LC-MS/MS analysis**
721 Mass spectrometry experiments were performed using an Orbitrap Eclipse Tribrid mass
722 spectrometer (Thermo Scientific, San Jose, CA) attached to an Acquity M-Class UPLC system
723 (Waters Corporation, Milford, MA). The UPLC system was set to a flow rate of 300 nL/min,
724 where mobile phase A was 0.2% formic acid in water and mobile phase B was 0.2% formic acid
725 in acetonitrile. The analytical column was prepared in-house with an I.D. of 100 microns pulled
726 to a nanospray emitter using a P2000 laser puller (Sutter Instrument, Novato, CA). The column

727 was packed with Dr. Maisch 1.9 micron C18 stationary phase to a length of approximately 25
728 cm. Peptides were directly injected into the column with a gradient of 3-45% mobile phase B,
729 followed by a high-B wash over a total of 80 minutes. The mass spectrometer was operated in a
730 data-dependent mode using CID fragmentation for MS/MS spectra generation.
731 The RAW data were analyzed using Byonic v5.2.5 (Protein Metrics, Cupertino, CA) to
732 identify peptides and infer proteins. Initial Byonic analyses used a concatenated FASTA file
733 containing the Uniprot *Saccharomyces cerevisiae* proteins and other likely contaminants and
734 impurities. Once sample complexity was determined, a second round of Byonic analyses was
735 completed using a targeted FASTA file, which included only the sequences present in the samples
736 and allowances for crosslinked peptides with the appropriate linker. Proteolysis with Trypsin/LysC
737 was assumed to be fully specific with up to two missed cleavage sites. The precursor ion tolerance
738 was set to 12 ppm. The fragment ion tolerance was set to 0.4 Da. Cysteine modified with
739 propionamide was set as a fixed modification in the search. Variable modifications included
740 oxidation on methionine and acetylation on protein N-terminus. Proteins were held to a false
741 discovery rate of 1% using the standard reverse-decoy technique.
742 The following procedure validated Potential crosslinked peptides using Byologic v5.2.31
743 (Protein Metrics). Given the number of possible crosslinked peptides observed in these
744 experiments, additional empirical constraints were applied to the potential crosslinked peptides to
745 produce a more rigorous validation set for comparison with other biochemical assays. For the BSG
746 cross-linking studies, crosslinked spectra were required to meet the following criteria: 1) all
747 peptides, crosslinked or native, were filtered to a <1% FDR; 2) precursor mass error of less than 7
748 ppm was required for crosslinked peptides, and 3) the peptide primary sequence was at least 6
749 amino acids in length for at least one of the crosslinked peptide pairs. For zero-length crosslinking
750 data analysis, the following additional constraints were added to those described above for BS3
751 crosslinking: 1) a minimum length of five amino acids was required for both members of the
752 crosslink; 2) an alternative 'XLink' algorithm from Byonic was used to make assignments based
753 on fragmentation of both peptides rather than just crosslink partner mass; 3) the crosslinks were
754 assumed valid only if the protein contained the lysine crosslink partner; and 4) at least two
755 crosslinked peptide spectra were assigned to the linkage. Following this, identified crosslinked
756 peptides were further categorized into three groups: high confidence, medium confidence, and low
757 confidence, where "high confidence" succeeded on all these rules and "low confidence" failed at
758 least in three of these rules.
759
760 **Preparation of y20S in the non-hydrolyzing condition**
761 The y20S complex consists of the Sso1–Snc1–Sec9 SNARE (ySNARE) complex, the
762 Sec18 oligomeric complex, and Sec17 adaptor proteins, and it was assembled in a multi-stage
763 workflow. Starting with the yeast exocytic complex, individual SNARE components Sec9 (401-
764 651), Sso1 (1-265), and Snc1 (1-93) were purified individually. All three proteins were cloned
765 into the pET28b plasmid vector with a 6x-His tag and a TEV cleavage sequence N-terminal to
766 the SNARE protein sequence.

767 For Sec9, we used a lysis buffer of pH 7.5, 50 mM NaPi, 300 mM NaCl, 10 mM
768 Imidazole, 0.5 mM TCEP, 1% Triton X-100 and SIGMAFAST Protease Inhibitor Cocktail
769 Tablet (Sigma-Aldrich S8830) which was used to resuspend bacterial cell pellets from an 8L
770 culture of auto-induced One Shot BL21 (DE3) *E*. coli (Thermofisher C600003). This
771 resuspended lysate was subjected to sonication for 20 minutes (3 seconds on, 9 seconds off, 60%
772 amplitude), followed by a 30-minute 4000 xg spin and a 1-hour 40,000 xg spin. The supernatant
773 was bound (1 hour, 4°C), run through a Ni-NTA column, and washed with pH 7.5, 50 mM NaPi,
774 30 mM Imidazole, 300 mM NaCl, and 0.5 mM TCEP buffer. The sample is then eluted with a
775 pH 8 50 mM NaPi, 400 mM Imidazole, 300 mM NaCl, and 0.5 mM TCEP buffer. This sample is
776 then digested overnight with TEV protease in a dialysis buffer (pH 8 20 mM Tris, 250 mM
777 NaCl, 0.5 mM TCEP, and 1 mM EDTA). The cleaved sample was then subjected to a MonoS
778 5/50 GL with buffer A consisting of pH 8 20 mM Tris, 50 mM NaCl, 0.5 mM TCEP, 1mM
779 EDTA and with buffer B consisting of pH 8 20 mM Tris, 500 mM NaCl, 0.5 mM TCEP, and
780 1mM EDTA. Taking the majority peak corresponding to Sec9, we then subjected this peak to
781 size exclusion chromatography (SEC) with the HiLoad 16/60 Superdex 200. The peak
782 corresponding to Sec9 was concentrated and flash-frozen. We followed the same protocol for
783 individually purifying Snc1 and Sso1.
784 Once all three individual SNAREs were purified, a 1:1:1 molar ratio of these proteins
785 was added to a 6M GdHCl solution. This solution was then slowly dialyzed overnight at 4°C into
786 a solution of 250 mM NaCl, 50 mM HEPES pH 7.6. This sample was then diluted to a NaCl
787 concentration of 75 mM and then subjected to MonoQ with the low salt buffer at 75 mM and the
788 high salt buffer at 500 mM with both buffers in 50 mM HEPES pH 7.6. The peak corresponding
789 to a 1:1:1 ratio of all three bands, indicative of the yeast exocytic complex, was then
790 concentrated for y20S formation without freezing.
791 The complete Sec18 protein coding sequence was cloned into the pMZ0002/pYK103
792 backbone with a 6x-His tag and TEV cleavage sequence N-terminal to Sec18. The 8L culture of
793 One Shot BL21 (DE3) *E.* coli (Thermofisher C600003) was spun down and resuspended in lysis
794 buffer of pH 7.5 100 mM HEPES, 500 mM KCl, 5 mM ATP, 5mM $MgCl_2$, protease inhibitor
795 tablets, and benzonase. This lysate was sonicated for 20 minutes (3 seconds on, 9 seconds off,
796 60% amplitude) and clarified with a 45,000 xg spin for 30 minutes. The lysate was supplemented
797 with 20 mM Imidazole bound to Ni-NTA beads (4°C) and washed with pH 7.5 20 mM HEPES,
798 480 mM KCl, 0.5 mM ATP, 0.5 mM TCEP, 20 mM Imidazole, 1 mM $MgCl_2$, and 10% glycerol.
799 The sample was then eluted with pH 7.5 20 mM HEPES, 480 KCl, 0.5 mM ATP, 0.5 mM TCEP,
800 500 mM Imidazole, 1 mM $MgCl_2$, and 10% glycerol. The protein-containing peak was then
801 equilibrated in SEC buffer pH 6.8 20 mM PIPES, 125 mM KCl, 0.2M sorbitol, 5 mM $MgCl_2$, 2
802 mM ATP, 2 mM DTT, and 10% glycerol and injected a HiLoad 16/60 Superdex 200. The
803 fractions were pooled, concentrated, and snap-frozen for later usage. The band right below Sec18
804 is an oligomeric *E. coli* contaminant, which is removed in the final steps of y20S complex
805 purification (**Figure S2A, C**). Moreover, this contaminant is absent in the protocol for preparing
806 high-purity Sec18 (see below and **Figure S6B**).

807 The full Sec17 coding sequence was cloned with a 10x-His tag and a TEV cleavage
808 sequence fused N-terminally. The 8L culture of One Shot BL21 (DE3) *E. coli* was spun down
809 and resuspended in a lysis buffer of pH 8 50 mM NaPi, 300 mM NaCl, 20 mM Imidazole, and
810 0.5 mM TCEP. This mixture was then sonicated (3 seconds on, 9 seconds off, 60% amplitude)
811 and clarified at 45,000 xg for 30 minutes. This supernatant was then incubated with Ni-NTA
812 beads for an hour and then washed with lysis buffer. The protein was eluted with lysis buffer
813 supplemented with 500 mM Imidazole and 5 mM EDTA. TEV protease was added to pooled
814 fractions and slowly dialyzed overnight at 4°C against a pH 8 50 mM Tris, 100 mM NaCl, 1 mM
815 EDTA, 0.5 mM TCEP buffer. This sample was then diluted to a NaCl concentration of 50 mM
816 and run on a MonoQ 10/100 from a 50 mM to 500 mM salt gradient. The major peak
817 corresponding to Sec17 was then pooled and injected into a HiLoad 16/60 Superdex 200 SEC.
818 The major peak from this run was taken, pooled, and snap-frozen for later usage.
819 To assemble the entire y20S complex, Sec17 was added to the freshly prepared yeast
820 exocytic SNARE complex, followed by EDTA quenched Sec18 with a final ratio of
821 Sec18:SNARE:Sec17 at 1:1.67:10, where a total of 5580 picomoles of Sec18 was used, in the
822 following buffer: pH 8 50mM Tris, 150 mM NaCl, 1 mM TCEP, 1 mM ATP, and 1 mM EDTA.
823 Following this assembly, this mixture was injected onto a Superose 6 10/300 increase column,
824 and the peak corresponding to the y20S complex, as assessed by elution volume and
825 corresponding SDS-PAGE gel, was concentrated to ~40 mg/mL.
826
827 **Single particle Cryo-EM grid preparation of y20S in the non-hydrolyzing condition**
828 Quantifoil R1.2/1.3 200 mesh gold grids were treated with chloroform and dried
829 overnight. Grids were glow discharged, and 5 microliters of the sample (at a final concentration
830 of 20 mg/mL with 0.05% v/v Nonidet P-40) was blotted onto the grids and further blotted and
831 vitrified in liquid ethane using an FEI Vitrobot (ThermoFisher Scientific). Grids were blotted for
832 4 seconds with a 5-second wait time (reduced to 3 seconds in hydrolyzing condition).
833
834 **Sample preparation and single particle Cryo-EM of y20S in the hydrolyzing condition**
835 Samples were prepared identically to y20S in the non-hydrolyzing condition, except that excess
836 $MgCl_2$ was blotted onto grids immediately before vitrification, and the total blot and wait time
837 was reduced to 7 seconds before freezing.
838
839 **Sample preparation and single particle Cryo-EM of substrate-free Sec18 in the hydrolyzing**
840 **condition**
841 An alternative protocol was required to prepare high-purity, substrate-free Sec18 since
842 low-purity Sec18, which can form y20S, was not amenable to high-quality cryo-EM studies.
843 Therefore, we used a different protocol for preparing NSF[10], except that at the final re-assembly
844 step, we used $MgCl_2$ instead of EDTA. The cryo-EM studies were performed similarly to the
845 studies of Y20S in the non-hydrolyzing condition.
846

847 **Sample preparation and single particle Cryo-EM of NSF in the hydrolyzing condition**
848 A sample of high-purity NSF was prepared, as described in the previous section. This
849 sample was exchanged into a buffer supplemented with 1mM magnesium chloride instead of
850 EDTA and incubated before a final SEC and freezing.
851
852 **Single particle cryo-EM data collection, processing, and model building**
853 Single particle cryo-EM data collection and processing workflow are described
854 thoroughly in the **Extended Table 1** and **Supplementary Figure 2**. An FEI Titan Krios
855 (ThermoFisher Scientific) cryo-electron microscope with either a K3 Gatan or a Falcon F4i
856 camera was used for data collection. Micrographs were analyzed using a combination of initial
857 Relion 3.1[52] processing followed by additional rounds of 3D classification or heterogenous
858 refinement, and final refinements in CryoSPARC v4[53]. A general workflow description is
859 provided in **Supplementary Figure 2,** and specific dataset information is provided in
860 **Supplementary Figures 2-6** as well.
861 y20S models were constructed by first docking the crystal structure of the exocytic
862 SNARE complex (PDB ID: 3B5N) and PDF/AlphaFold2[54] models for Sec17 (1QQE/AF-
863 P32602-F1-v4) into the unsharpened density first obtained in Relion 3.1[52]. Next, sharpened
864 cryoSPARC-v4[53] maps were used to model the Sec18 complex and the region of Sso1 that
865 extended from the spire into the D1 pore. For class 1, 3DFlex analysis in cryoSPARC-v4 was
866 performed. A mixture of the Relion 3.1 and cryoSPARC-v4 unsharpened and sharpened maps,
867 and the 3Dflex map were used to model the domain outside of the D2 ring. The resulting atomic
868 models were iteratively refined with a combination of COOT[55], Phenix real-space refinement[56],
869 and ISOLDE[57].
870 Substrate-free Sec18 and NSF models were built *de novo* in COOT using cryoSPARC
871 sharpened maps and iteratively refined with ISOLDE and Phenix. AlphaFold2 model of Sec18
872 was used as a starting reference for model building (AF-P18759-F1-v4).
873
874 **Structural and conformational analysis**
875 Statistical structural analysis was performed to identify the most significant backbone
876 motions between the different structural states of Sec18 without substrate, as observed in Figure
877 6. Using Python 3, principal component analysis (PCA) on backbone ϕ/ψ angles was performed,
878 and the single mode that contributed most to the variance (>70%) was analyzed. y20S models
879 were then clustered in this reduced 5-dimensional space. When comparing the substrate-free and
880 substrate-engaged states, ensembles consistent with a given map were generated to avoid model-
881 building bias using Phenix's simple molecular dynamics implementation for 2000 steps followed
882 by a round of phenix.refine[56]. These ensembles were then subjected to backbone ϕ/ψ PCA, and
883 the mode that contributed to the largest variance between the two clusters for the two classes was
884 used to determine which residues contributed most to the difference in structures. For more
885 details, please see the conformational tool package deposited in GitHub for annotated and
886 commented code (https://github.com/YousufAKhan/ConformationalAnalysis/).

887
888
889 **smFRET disassembly/re-assembly assay**
890 smFRET assays with linked neuronal SNAREs, NSF, α-SNAP, and reagents were
891 prepared, as previously reported[11]. Briefly, linked SNARE complex (L-SNARE) composed of
892 SNAP25A, synaptobrevin-2, and syntaxin-1A were biotinylated and flowed onto the chamber
893 that was passivated by 10 mg/mL egg phosphatidylcholine 50 nm liposomes coated with 1
894 mg/mL of biotinylated BSA to mimic the lipid environment inside the cell. 0.1 mg/mL
895 streptavidin was added to surface-tether the biotinylated and labeled L-SNARE complexes. L-
896 20S was then assembled by first adding αSNAP and then later NSF (if in disassembly
897 conditions). L-SNARE was diluted such that about 500 molecules of L-SNARE per 45 x 90 μm^2
898 field of view were visible. The labels for the Habc domain are at residue positions 35 and 105,
899 and labels for the L-SNARE complex are at residue position 249 of syntaxin and residue position
900 82 of synaptobrevin, identical to a previous study[11]. The Habc label positions are at the tips of
901 the α-helices that are positioned away from the D2 pore and the Sec18 complex (Fig. 5a). Thus,
902 one would expect that 20S complex formation does not affect the quantum yield and
903 conformational dynamics of the dyes, which is indeed what we observe. The labeling was
904 performed by mutating the residues at these positions to cysteines and stochastic conjugation
905 with Alexa 555 and Alexa 647 dyes.
906
907 All smFRET experiments were performed on a prism-type total internal reflection
908 fluorescence (TIRF) microscope using 532 nm (green) laser (CrystaLaser) excitation. Two
909 observation channels were created by a 640 nm single-edge dichroic beamsplitter (FF640-FDi01-
910 25x36, Shemrock): one channel was used for the fluorescence emission intensity of the Alexa
911 555 dye and the other channel for the Alexa 647 dye. The two channels were recorded on two
912 adjacent rectangular areas (45 × 90 μm2) of a charge-coupled device (CCD) camera (iXon+ DV
913 897E, Andor Technology USA, South Windsor CT). The imaging data were recorded with the
914 smCamera program (Taekjip Ha, Johns Hopkins University, Baltimore). Flow chambers were
915 assembled by creating a "sandwich" consisting of a quartz slide and a glass coverslip that were
916 both coated with polyethylene glycol (PEG) molecules consisting of 0.1% (w/v) biotinylated-
917 PEG except when stated otherwise and using double-sided tape to create up to five flow
918 chambers.
919
920 Fluorescence intensity time traces were recorded by the smCamera[58] program, peaks
921 were selected, and correlated in the two channels as previously described[19]. The time traces were
922 imported into tMaven[51] for smFRET analysis. The standard, recommended tMaven workflow
923 was employed. In short, all traces were evaluated manually and not subject to any automated
924 trace preprocessing in tMaven. Traces that did not have single photobleaching events were not
925 considered. After obtaining all traces that fit these criteria, the automatic photobleaching
926 algorithm was used to remove regions that were photobleached for analysis of the FRET states.

927 Following this, the vbGMM model was used to model the transition between states with an
928 assumption of two states (i.e., high and low). Following this, the tMaven "one dimension
929 histogram" tool was used to generate histograms of the distribution of states of the raw FRET
930 efficiency $E=I_A / (I_A+I_D)$, where I_A and I_D are the acceptor and donor fluorescence intensities,
931 respectively; no corrections for bleed-through, detection efficiency, and quantum yield were
932 applied.
933
934 **Crosslinking assays**
935 Cysteines were introduced into Sec9 and Sso1 for labeling with Oregon Green Maleimide
936 488 (O6034). UAG stop codons were introduced at V57 and F83 in Sso1 for crosslinking. Cys-
937 Sec9, Cys-Sso1 (with or without stop codon depending on if used for crosslinked), and 6x-His-
938 TEV-Snc1 were co-expressed (if crosslinked, also transformed with pEVOL-pAzF AddGene
939 #31186, 2mM AzF and 0.2% v/v arabinose) and induced with IPTG. Cell pellets were lysed with
940 pH 7 50 mM Tris, 200 mM NaCl, 1% v/v Triton X-100, 20 mM Imidazole, 0.5 mM TCEP and
941 protease inhibitor tablets. Lysate was sonicated for 20 minutes (3 seconds on, 9 seconds off, 60%
942 amplitude) and then clarified at 40,000 xg for 30 minutes. Following a 1-hour incubation at 4°C,
943 the beads were washed with two different buffers. Buffer 1 is simply a lysis buffer without
944 Triton X-100, and Buffer 2 is a high salt wash of pH 7 50 mM Tris, 1M NaCl, 50 mM Imidazole,
945 0.5 mM TCEP. The complex was eluted with pH 7 50 mM Tris, 200 mM NaCl, 350 mM
946 Imidazole, and 0.5 mM TCEP. The sample was then digested overnight with TEV protease and
947 dialyzed into pH 7 20 mM Tris, 200 mM NaCl, 0.5 mM TCEP. This sample was then injected
948 onto a HiLoad 16/60 Superdex 200. The fractions containing all three in equimolar ratios were
949 taken and concentrated. Samples were labeled with Oregon Green Maleimide 488 in molar
950 excess overnight before cleanup with a Zeba spin column (ThermoFisher 89889). If the sample
951 was meant to be crosslinked, it was subjected to UV irradiation before Oregon Green Maleimide
952 labeling. The buffers used for these crosslinking assays were the same as the final dialysis buffer
953 but were degassed before UV irradiation and Oregon Green Maleimide labeling.
954 For native gel disassembly assays, reactions were assembled in test tubes, initiated with
955 $MgCl_2$, and quenched with EDTA. Samples were then loaded into Any kD Mini-Protean gels
956 (Bio-Rad 4569033) and used Tris-glycine running buffer (Bio-Rad) supplemented with 1 mM
957 ATP to prevent Sec18 from falling apart in the gel. Gels were first visualized in an iBright 1500
958 (ThermoFisher Scientific) to visualize ySNARE bands only before coomassie staining. Gel
959 densitometry was assessed in ImageJ.
960
961 **FRET and fluorescent dequenching disassembly assays**
962 Neuronal disassembly assays were carried out as previously reported[10], leveraging
963 fluorescence dequenching of the neuronal SNARE complex labeled with Oregon Green
964 Maleimide 488. For yeast SNARE disassembly assays, a strategy was devised to tag Snc1 with
965 mTurq and Sso1 with mVenus. When assembled, excitation by a 434 nm laser leads to mVenus
966 emission. 434 nm laser excitation leads to mTurq emission. Disassembly is followed by
967 monitoring excitation/emission at 434/474 nm such that as the SNARE complex is disassembled,

968 mTurq emission increases. We used the same instrument (FlexStation II 384, Molecular Devices)
969 and a 384-well format to perform both the dequenching and FRET assays that were initiated by
970 titrating $MgCl_2$ in excess of the reactions.
971
972 **Vacuolar fusion assay**
973 Assays were performed as previously reported[41,42] with the same substrate-free Sec18
974 protein sample/batch that was purified and used for Cryo-EM. Briefly, proteoliposomes with
975 vacuolar SNAREs were prepared with either Phycoerythirin-biotin (PhycoE) or Cy5 and
976 incubated in a fluorescence plate reader for 40 minutes. FRET between PhycoE and Cy5 was
977 measured at 1-minute intervals. Reaction mixtures contained HOPS complex, Sec17, and
978 variable amounts of Sec18.
979
980 **Data availability statement**
981 The mass spectrometry proteomics data have been deposited to the ProteomeXchange
982 Consortium via the PRIDE partner repository (https://www.ebi.ac.uk/pride/) with the dataset
983 identifier PXD062002 and 10.6019/PXD062002. All cryo-EM maps and coordinates have been
984 deposited in the EMDB and PDB, respectively. The codes for the following classes (PDB/EMD)
985 - Y20S non-hydrolyzing condition
986 - Class 1
987 - 9CRU/EMD-45883
988 - Class 2
989 - 9N22/EMD-48826
990 - Class 3
991 - 9CRX/EMD-45885
992 - Class 4
993 - 9NG2/EMD-49380
994 - Class 5
995 - 9NLU/EMD-49522
996 - Class 6
997 - 9NLW/EMD-49524
998 - Class 7
999 - 9NLY/EMD-49526
1000 - Class 8
1001 - 9NLZ/EMD-49527
1002 - Class 9 (All merge, focus on D1/D2)
1003 - 9NM1/EMD-49528
1004 - Y20S hydrolyzing condition
1005 - Class 1
1006 - No model created/EMD-70472
1007 - Class 2

1008 ▪ 9NUD/EMD-49801
1009 ○ Class 3
1010 ▪ 9NUE/EMD-49802
1011 ○ Class 4
1012 ▪ 9NUZ/EMD-49824
1013 • Sec18 hydrolyzing condition
1014 ○ Class 1
1015 ▪ 9NV1/EMD-49826
1016 ○ Class 2
1017 ▪ 9NV0/EMD-49825
1018 • NSF hydrolyzing condition
1019 ○ Class 1
1020 ▪ 9NV9/EMD-49831
1021 ○ Class 2
1022 ▪ 9NVD/EMD-49833
1023
1024 The smFRET data have been deposited in the Stanford Data Repository
1025 (https://purl.stanford.edu/bm031pm6709). All data are available with the manuscript online and
1026 materials can be obtained from AddGene.org, where all the constructs will be deposited.
1027

1028 **Software and code availability**

1029 The conformational tool package has been deposited in GitHub at
1030 https://github.com/YousufAKhan/ConformationalAnalysis and smFRET related scripts can be
1031 found at https://github.com/brungerlab/single_molecule_matlab_scripts.

1032

1033 **Methods-only references**

1034

1035 52. Scheres, S. H. W. A Bayesian view on cryo-EM structure determination. *J. Mol. Biol.* **415**,
1036 406–418 (2012).
1037 53. cryoSPARC: algorithms for rapid unsupervised cryo-EM structure determination - PubMed.
1038 https://pubmed.ncbi.nlm.nih.gov/28165473/.

1039 54. Jumper, J. *et al.* Highly accurate protein structure prediction with AlphaFold. *Nature* **596**,
1040 583–589 (2021).
1041 55. Emsley, P. & Cowtan, K. Coot: model-building tools for molecular graphics. *Acta*
1042 *Crystallogr. D Biol. Crystallogr.* **60**, 2126–2132 (2004).
1043 56. Adams, P. D. *et al.* The Phenix Software for Automated Determination of Macromolecular
1044 Structures. *Methods San Diego Calif* **55**, 94–106 (2011).
1045 57. Croll, T. I. ISOLDE: a physically realistic environment for model building into low-
1046 resolution electron-density maps. *Acta Crystallogr. Sect. Struct. Biol.* **74**, 519–530 (2018).
1047 58. Lee, K. S. & Ha, T. smCamera: all-in-one software package for single-molecule data
1048 acquisition and data analysis. *J. Korean Phys. Soc.* **86**, 1–13 (2025).
1049 59. McCann, J. J., Choi, U. B., Zheng, L., Weninger, K. & Bowen, M. E. Optimizing Methods to
1050 Recover Absolute FRET Efficiency from Immobilized Single Molecules. *Biophys. J.* **99**,
1051 961–970 (2010).
1052

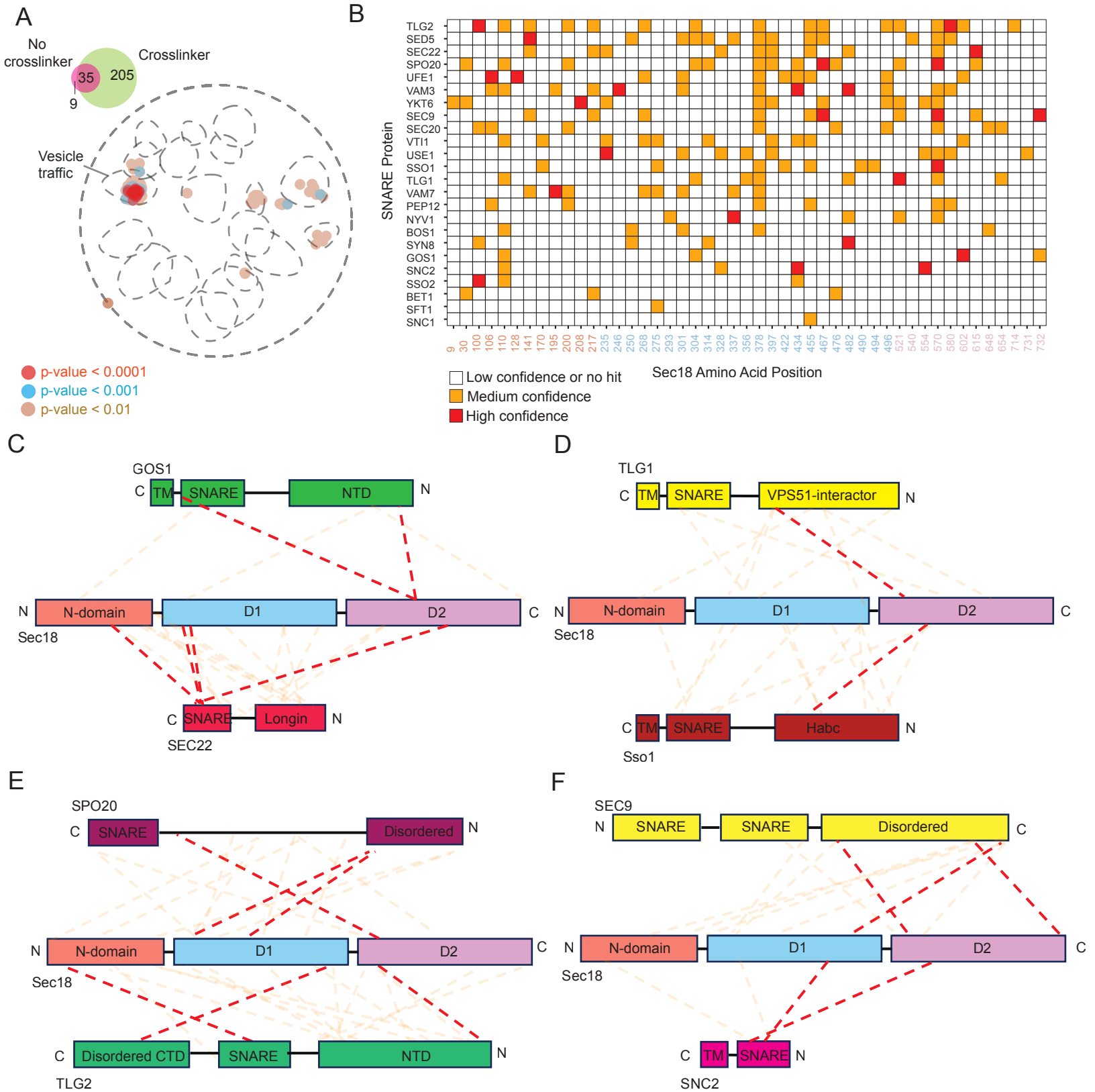
A
No crosslinker
Crosslinker
35
205
9
Vesicle traffic
p-value < 0.0001
p-value < 0.001
p-value < 0.01
B
SNARE Protein
TLG2
SED5
SEC22
SPO20
UFE1
VAM3
YKT6
SEC9
SEC20
VTI1
USE1
SSO1
TLG1
VAM7
PEP12
NYV1
BOS1
SYN8
GOS1
SNC2
SSO2
BET1
SFT1
SNC1
Sec18 Amino Acid Position
Low confidence or no hit
Medium confidence
High confidence
C
GOS1
TM
SNARE
NTD
N-domain
D1
D2
Sec18
SNARE
Longin
SEC22
D
TLG1
TM
SNARE
VPS51-interactor
N-domain
D1
D2
Sec18
TM
SNARE
Habc
Sso1
E
SPO20
SNARE
Disordered
N-domain
D1
D2
Sec18
Disordered CTD
SNARE
NTD
TLG2
F
SEC9
SNARE
SNARE
Disordered
N-domain
D1
D2
Sec18
TM
SNARE
SNC2

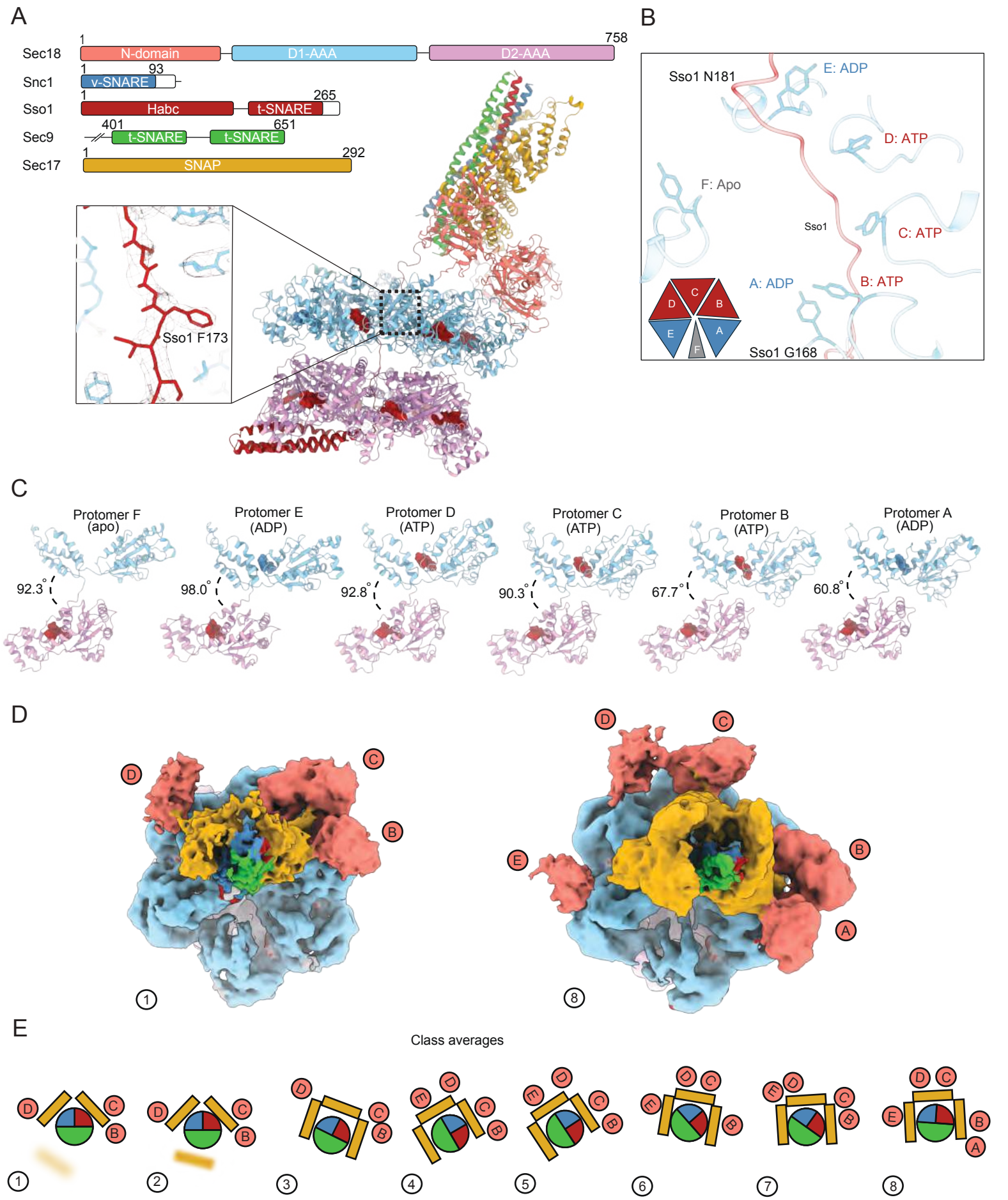
A
Sec18
N-domain
D1-AAA
D2-AAA
1
758
Snc1
v-SNARE
1
93
Sso1
Habc
t-SNARE
1
265
Sec9
t-SNARE
t-SNARE
401
651
Sec17
SNAP
1
292
Sso1 F173
B
Sso1 N181
E: ADP
D: ATP
F: Apo
Sso1
C: ATP
A: ADP
B: ATP
Sso1 G168
C
Protomer F (apo)
Protomer E (ADP)
Protomer D (ATP)
Protomer C (ATP)
Protomer B (ATP)
Protomer A (ADP)
92.3°
98.0°
92.8°
90.3°
67.7°
60.8°
D
E
Class averages

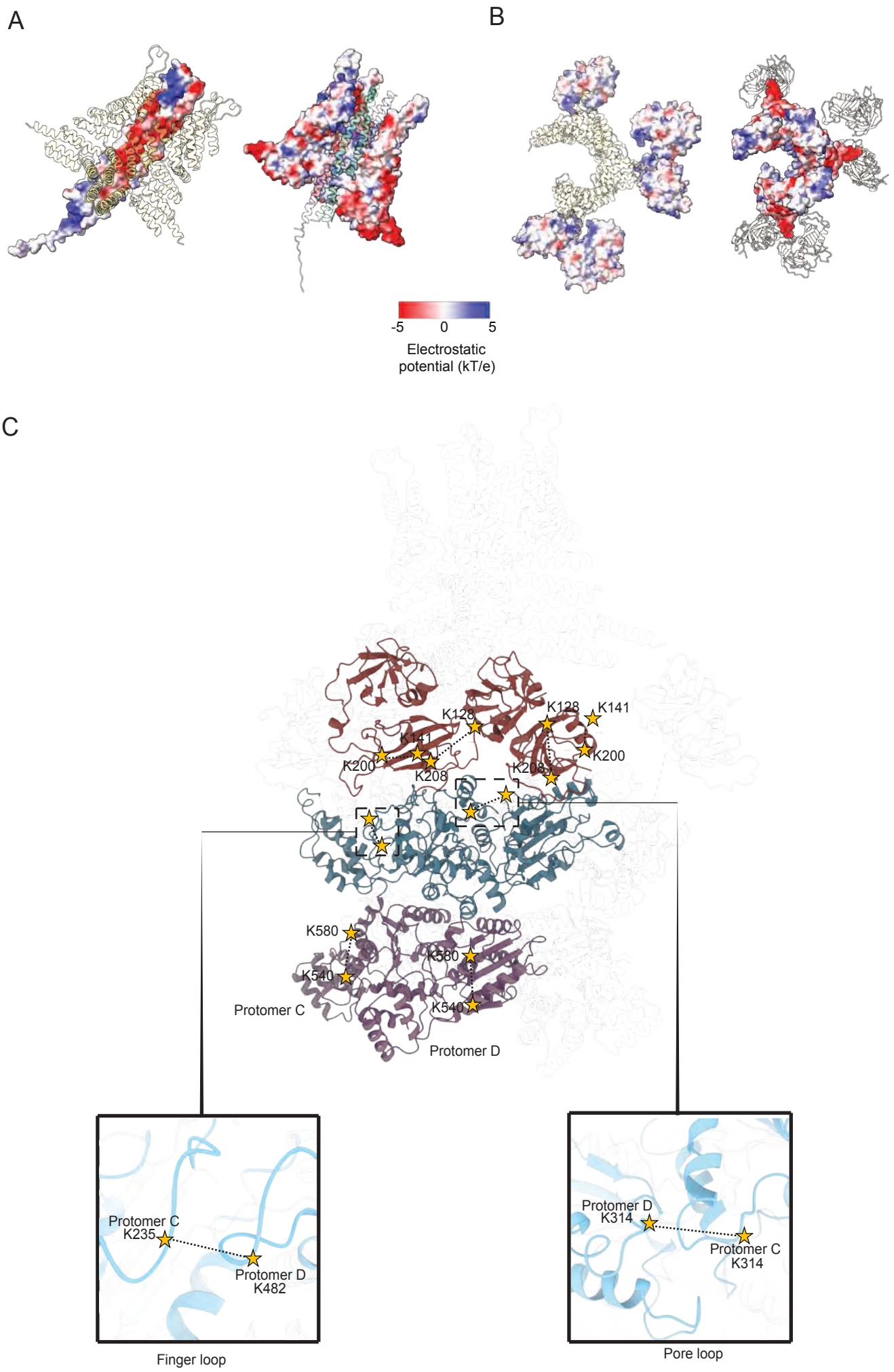
A
B
-5
0
5
Electrostatic potential (kT/e)
C
K128
K141
K200
K208
K128
K141
K200
K208
K580
K540
K580
K540
Protomer C
Protomer D
Protomer C
K235
Protomer D
K482
Finger loop
Protomer D
K314
Protomer C
K314
Pore loop

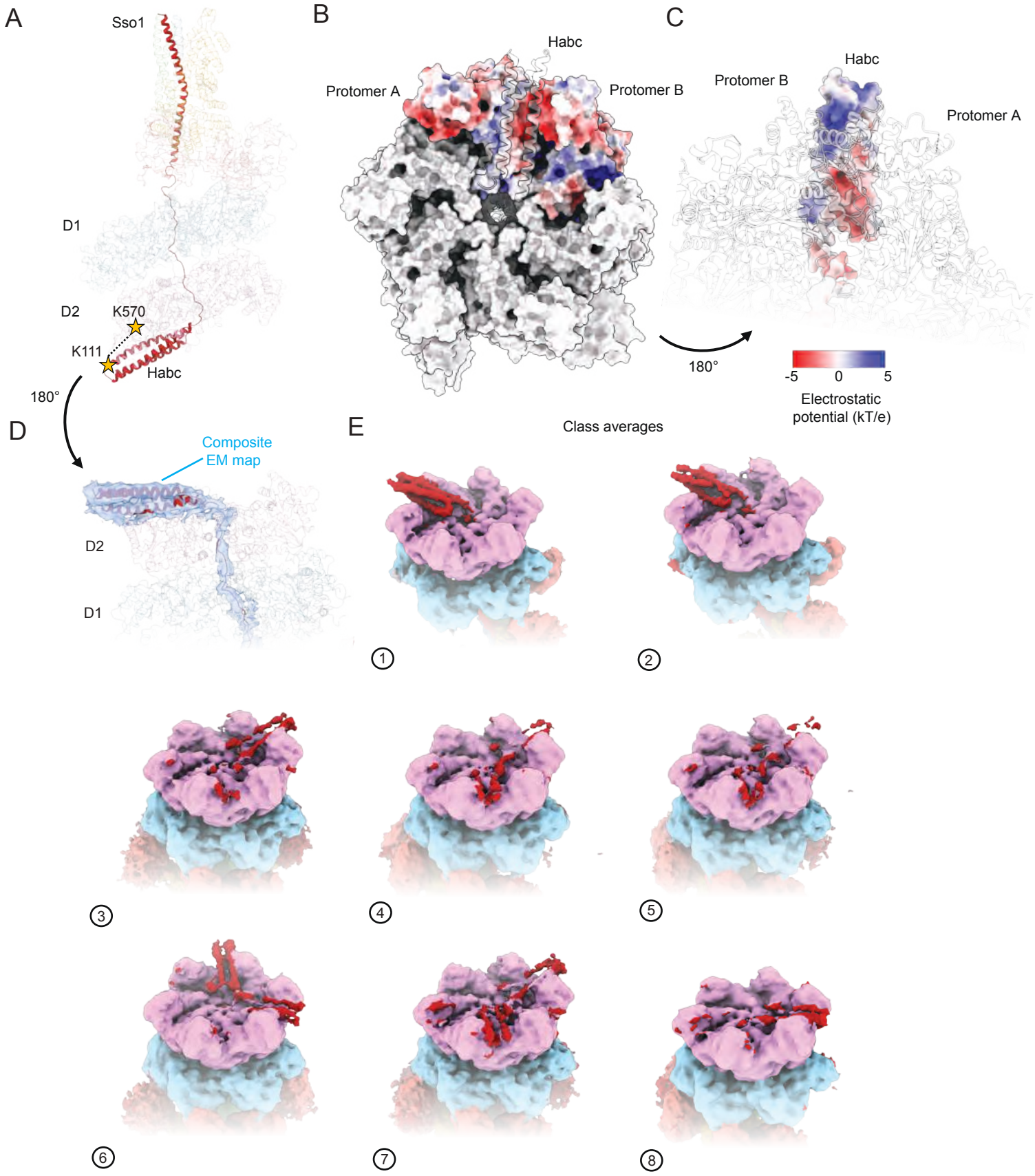
A
Sso1
D1
D2
K570
K111
Habc
180°
B
Habc
Protomer A
Protomer B
C
Habc
Protomer B
Protomer A
180°
-5
0
5
Electrostatic potential (kT/e)
D
Composite EM map
D2
D1
E
Class averages
1
2
3
4
5
6
7
8

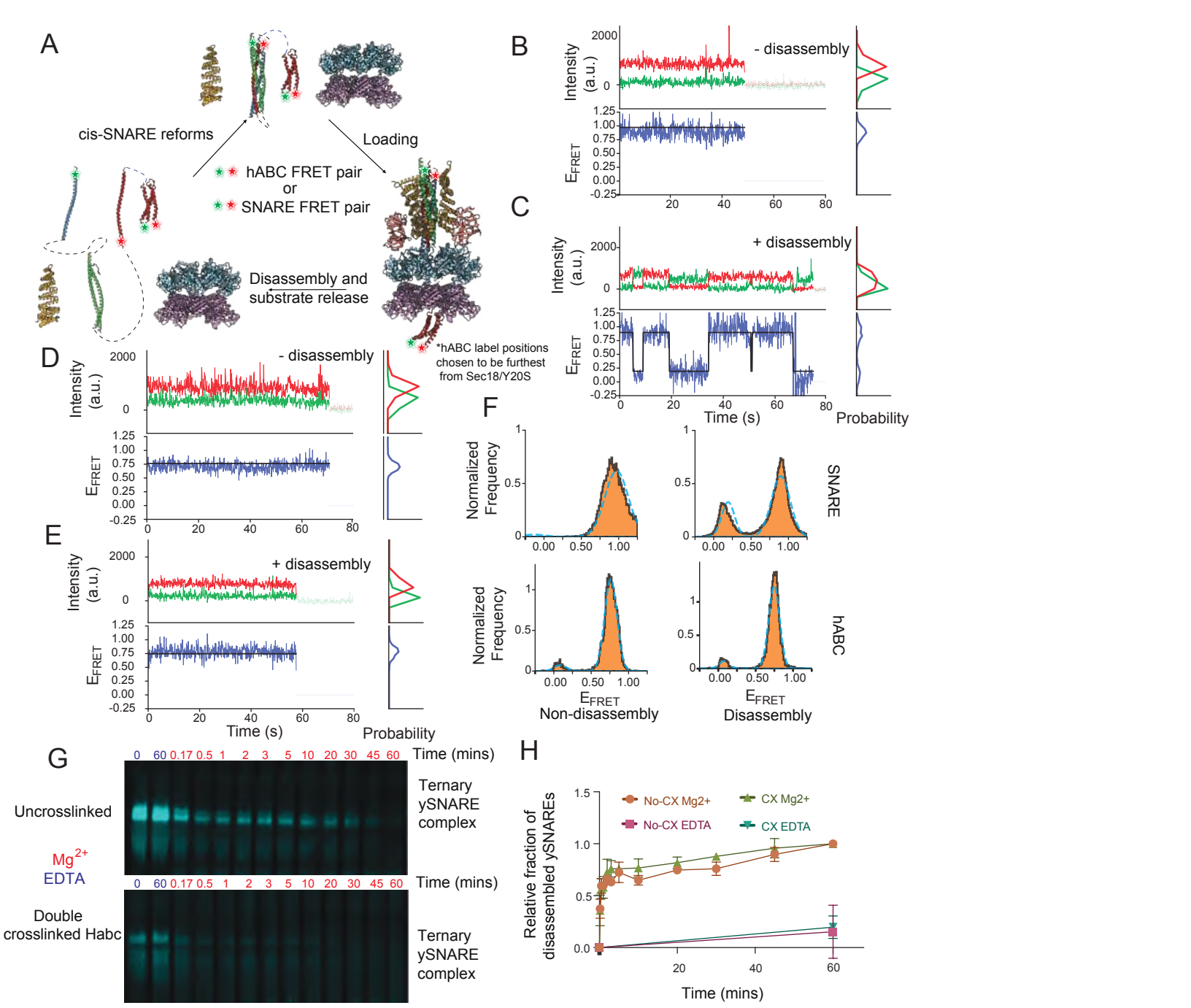
A
cis-SNARE reforms
Loading
hABC FRET pair
or
SNARE FRET pair
Disassembly and
substrate release
*hABC label positions
chosen to be furthest
from Sec18/Y20S
B
- disassembly
Intensity (a.u.)
E_FRET
C
+ disassembly
Time (s)
Probability
D
- disassembly
E
+ disassembly
Time (s)
Probability
F
Normalized Frequency
SNARE
hABC
E_FRET
Non-disassembly
Disassembly
G
Time (mins)
Uncrosslinked
Mg2+
EDTA
Double
crosslinked Habc
Ternary
ySNARE
complex
H
Relative fraction of
disassembled ySNAREs
No-CX Mg2+
CX Mg2+
No-CX EDTA
CX EDTA
Time (mins)

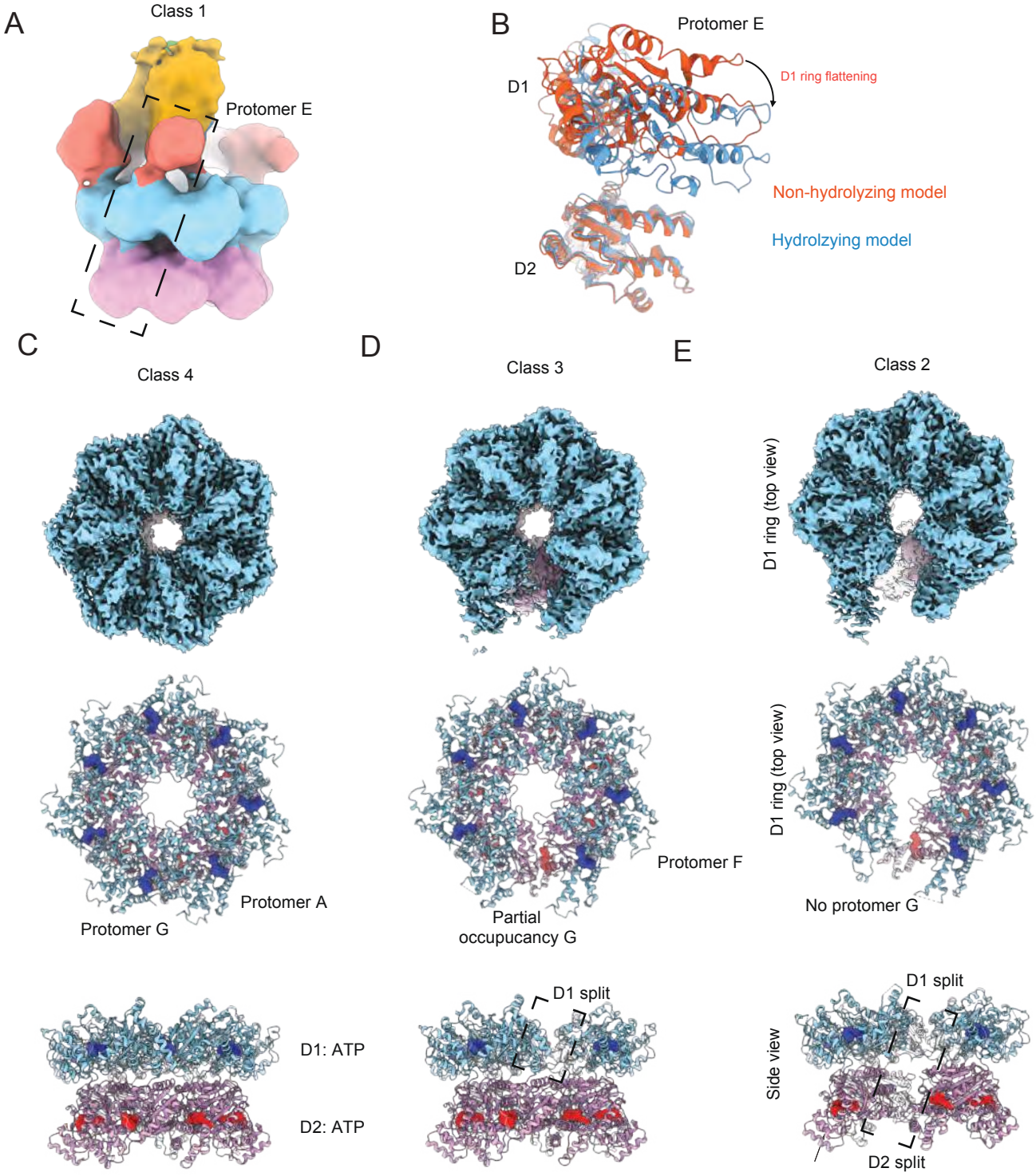
A
Class 1
Protomer E
B
Protomer E
D1
D1 ring flattening
Non-hydrolyzing model
Hydrolzying model
D2
C
Class 4
Protomer A
Protomer G
D1: ATP
D2: ATP
D
Class 3
Protomer F
Partial
occupucancy G
D1 split
E
Class 2
D1 ring (top view)
D1 ring (top view)
No protomer G
D1 split
Side view
D2 split

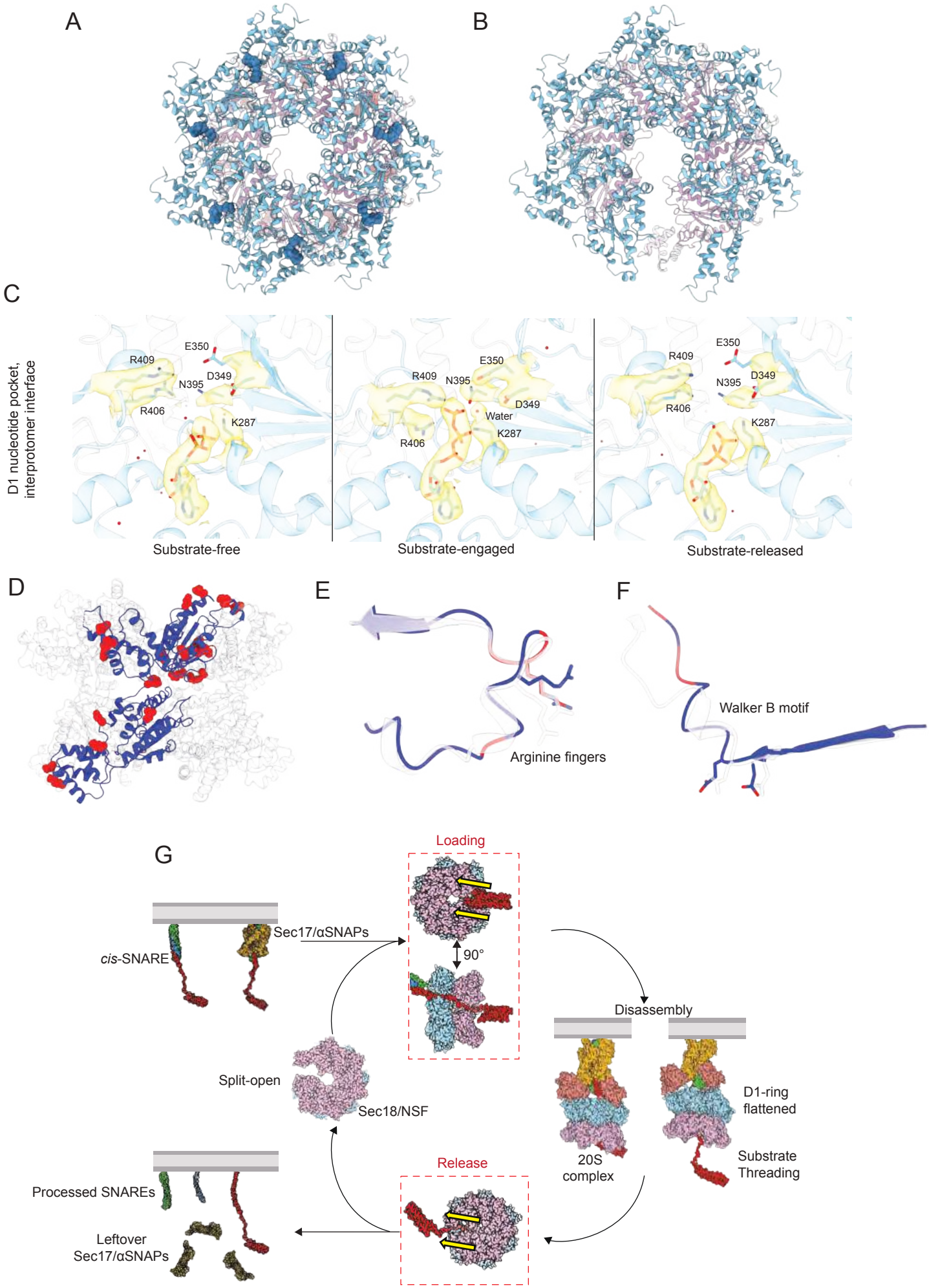
A
B
C
D1 nucleotide pocket, interprotomer interface
E350
R409
D349
N395
R406
K287
Water
Substrate-free
Substrate-engaged
Substrate-released
D
E
Arginine fingers
F
Walker B motif
G
Loading
Sec17/αSNAPs
cis-SNARE
90°
Disassembly
Split-open
Sec18/NSF
D1-ring flattened
20S complex
Substrate Threading
Release
Processed SNAREs
Leftover Sec17/αSNAPs

A

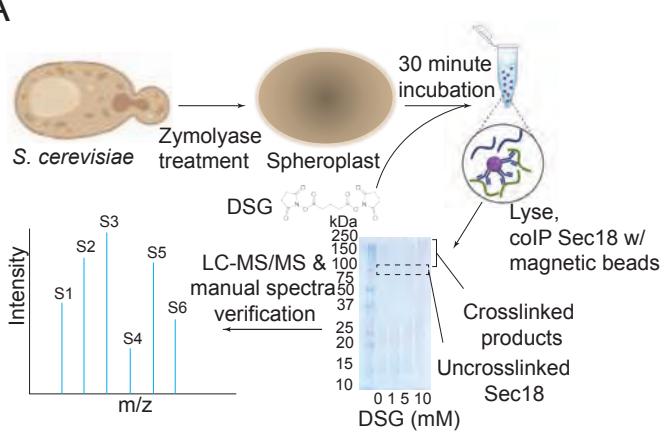
S. cerevisiae
Zymolyase treatment
Spheroplast
30 minute incubation
DSG
Lyse, coIP Sec18 w/ magnetic beads
kDa
250
150
100
75
50
37
25
20
15
10
0 1 5 10
DSG (mM)
Crosslinked products
Uncrosslinked Sec18
LC-MS/MS & manual spectra verification
Intensity
S1
S2
S3
S4
S5
S6
m/z

B

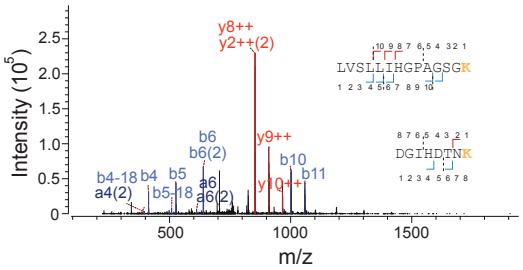
Intensity (10^5)
2.5
2.0
1.5
1.0
0.5
0
500
1000
1500
m/z
y8++
y2++(2)
LVSLLIHGPAGSGK
b6
b6(2)
y9++
b10
b11
b4-18
b4
b5
a4(2)
b5-18
a6
a6(2)
y10++
DGTHDTNK

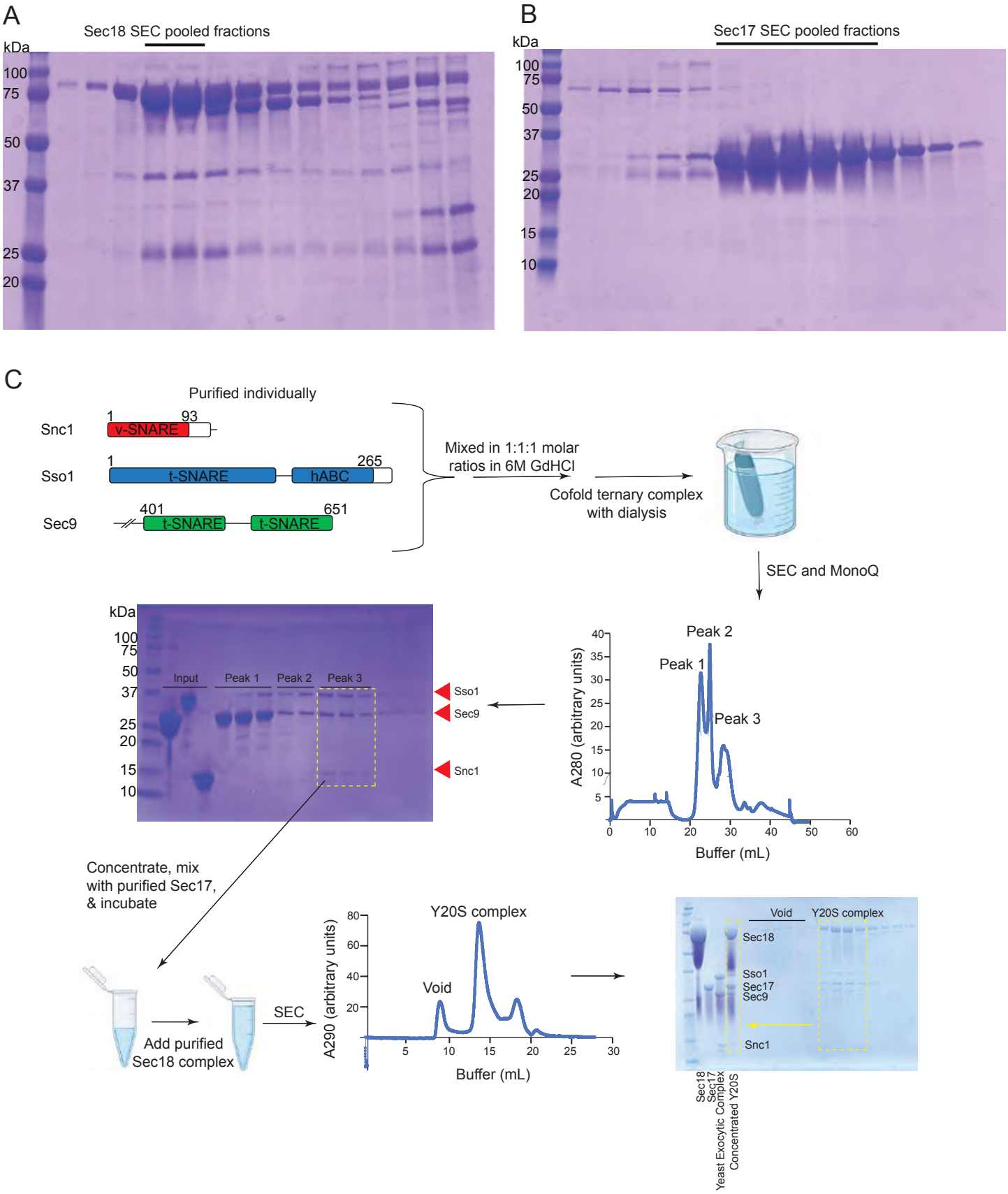
A
Sec18 SEC pooled fractions
kDa
100
75
50
37
25
20
B
Sec17 SEC pooled fractions
kDa
100
75
50
37
25
20
15
10
C
Purified individually
Snc1
1
93
v-SNARE
Sso1
1
265
t-SNARE
hABC
Sec9
401
651
t-SNARE
t-SNARE
Mixed in 1:1:1 molar ratios in 6M GdHCl
Cofold ternary complex with dialysis
SEC and MonoQ
kDa
Input
Peak 1
Peak 2
Peak 3
Sso1
Sec9
Snc1
A280 (arbitrary units)
Buffer (mL)
Concentrate, mix with purified Sec17, & incubate
Add purified Sec18 complex
SEC
A290 (arbitrary units)
Y20S complex
Void
Buffer (mL)
Void
Y20S complex
Sec18
Sso1
Sec17
Sec9
Snc1
Sec18
Sec17
Yeast Exocytic Complex
Concentrated Y20S

A

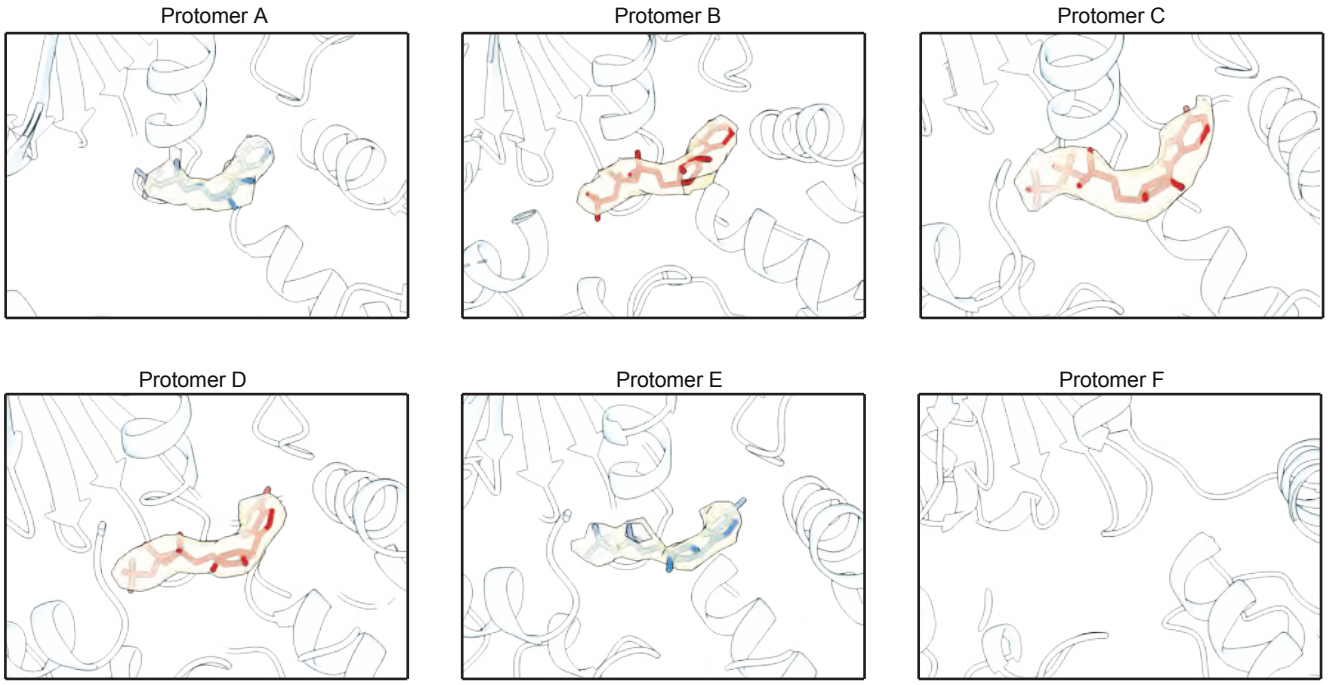
Protomer A
Protomer B
Protomer C
Protomer D
Protomer E
Protomer F

B

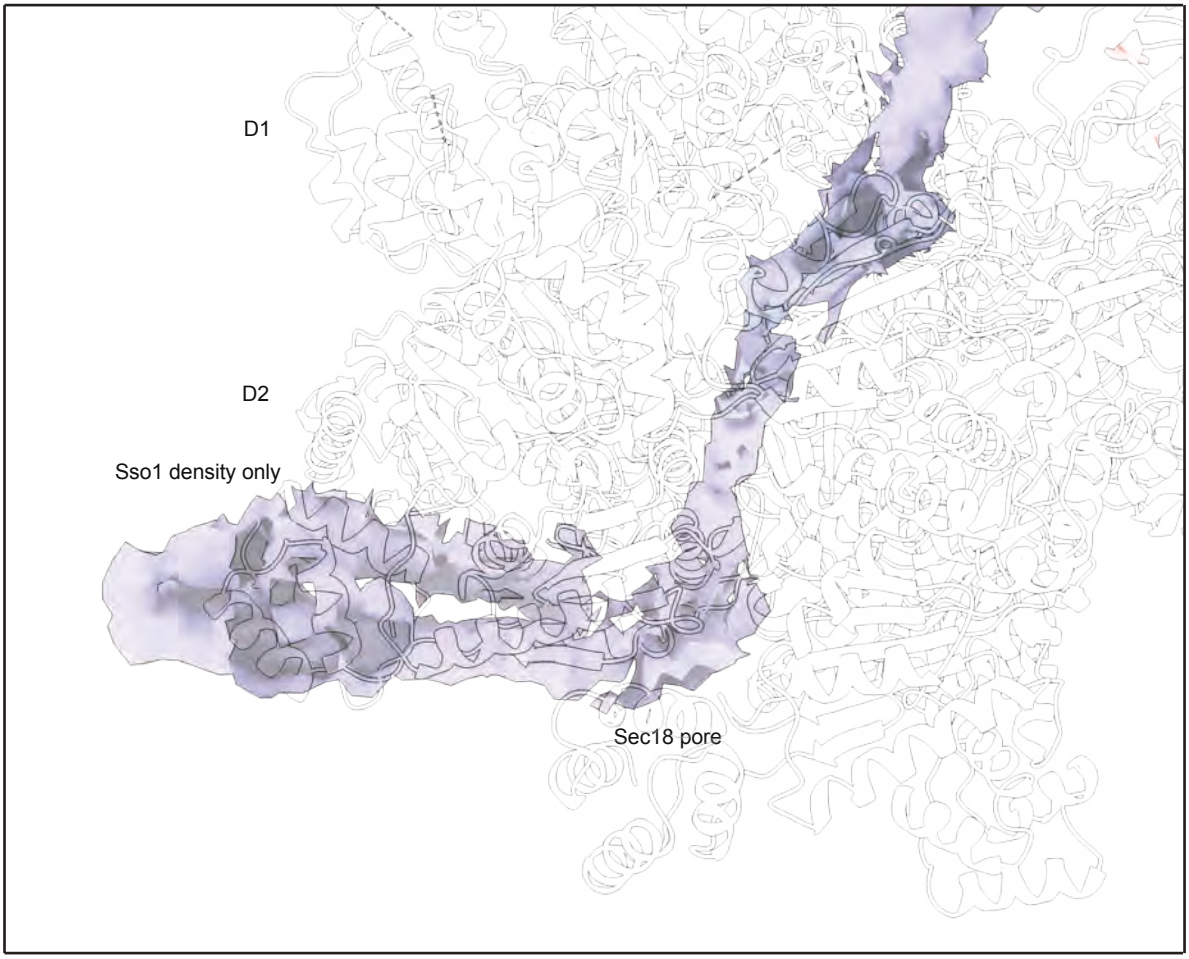
D1
D2
Sso1 density only
Sec18 pore

A

```
Sec18/1-758   1 MFKIPGFGKAAANHTPPDMTNMDTRTRHLKVSNCPNNSYALANVAAVSPNDFPNNIYIII----DNLFVFTTRHSNDIPPGTIGFNGNQRTWGGWSL  93
NSF/1-744     1 ----------------------MAGRSMQAARCPTDELSLSNCAVVSEKDYQSGQHVIVRTSPNHKYIFTLRTHPSVVPGSVAFSLPQRKWAGLSI  74

Sec18/1-758  94 NDDVQAKAFDLFKYSGKQSYLGSIDIDISFRARGKAVSTVFDQDELAKQFVRCYESDIFSPTDYLIMEFQGHFFDLKIRNVQAIDLGDIEPTSA--V 188
NSF/1-744    75 GQEIEVA---LYSFDKAKQCIGTMTIEIDFLQKKNIDSNPYDTDKMAAEFIQQFNNQAFSVGQQLVFSFNDKLFGLLVKDIEAMDPSILKGEPASGK 168

Sec18/1-758 189 ATGIETKGILTKQTDINFFKGRDGLVNLKSSNSLRPRSNAVIRPDFKFEDLGVGGLDKEFTKIFRRAFASRIFPPSVIEKLGISHVKGLLLYGPPGT 285
NSF/1-744   169 RQKII-EVGLVVGNSDVAFEKAENSSLNLIGKAKTKENRQSIINPDWNFEKMGIGGLDKEFSDIFRRAFASRVFPPEIVEQMGCKHVKGILLYGPPGC 264

Sec18/1-758 286 GKTLIARKIGTMLNAKEPKIVNGPEILSKYVGSSEENIRNLFKDAEAEYRAKGEESSLHIIIFDELDSVFKQRGSRGDGTGVGDNVVNQLLAKMDGV 382
NSF/1-744   265 GKTLLARQIGKMLNAREPKVVNGPEILNKYVGESEANIRKLFADAEEEQRRLGANSGLHIIIFDEIDAICKQRGSMAGSTGVHDTVVNQLLSKIDGV 361

Sec18/1-758 383 DDLNNILVIGMTNRKDLIDSALLRPGRFEVQVEIHLPDEKGRLQIFDIQTKKMRENNMMSDDVNLAELAALTKNFSGAEIEGLVKSASSFAINKTVN 479
NSF/1-744   362 EDLNNILVIGMTNRPDLIDEALLRPGRLEVKMEIGLPDEKGRLQILHIHTARMRGHQLLSADVDIKELAVETKNFSGAELEGLVRAAQSTAMNRHIK 458

Sec18/1-758 480 IGKGATKLNTKDIAKLKVTREDFLNAL-NDVTPAFGISEEDLKTCVEGGMMLYSERVNSILKNGARYVRQVRESDKSRLVSLLIHGFAGSGKTALAA 575
NSF/1-744   459 ASTK-VEVDMEKAESLQVTRGDFLASLENDIKPAFGTNQEDYASYIMNGIIKWGDPVTRVLDDGELLVQQTKNSDRTPLVSVLLEGPPHSGKTALAA 554

Sec18/1-758 576 EIALKSGFPFIRLISPNELSGMSESAKIAYIDNTFRDAYKSPLNILVIDSLETLVDWVPIGPRFSNNILQMLKVALKRKPPQDRRLLIMTTTSAYSV 672
NSF/1-744   555 KIAEESNFPFIKICSPDKMIGFSETAKCQAMKKIFDDAYKSQLSCVVVDDIERLLDYVPIGPRFSNLVLQALLVLLKKAPPQGRKLLIIGTTSRKDV 651

Sec18/1-758 673 LQQMDILSCFDNEIAVPNMTNLDELNNVMI-ESNFLDDAGRVKVINELSRSCPNFNVGIKKTLTNIETARH--DEDPVNELVELMTQSA-------  758
NSF/1-744   652 LQEMEMLNARSTTIHVPNIATGEQLLEALELLGNFKD-KERTTIAQQV--KGKKVWIGIKKLLMLIEMSLQMDPEYRVRKFLALLREEGASPLDFD  744
```

B

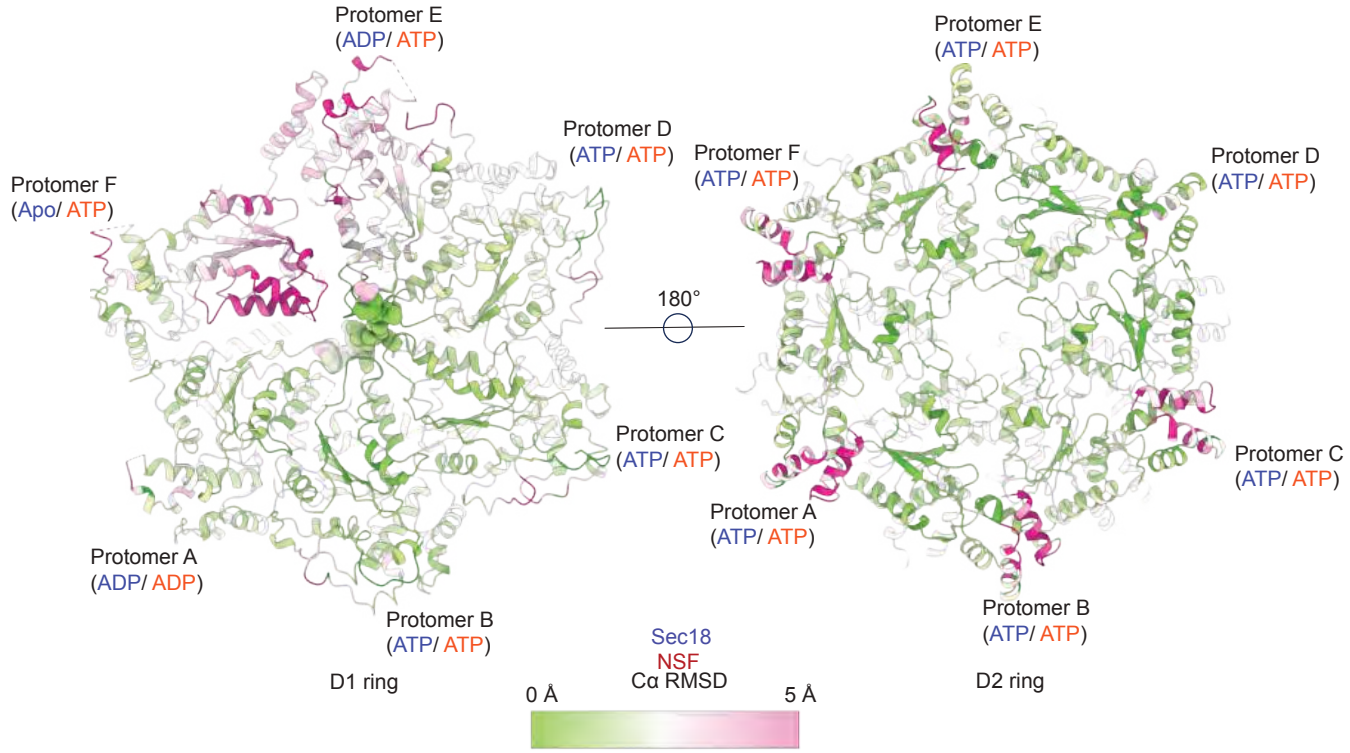

C

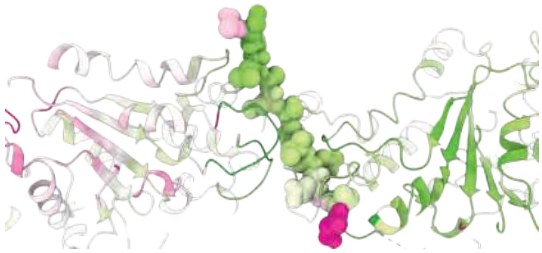

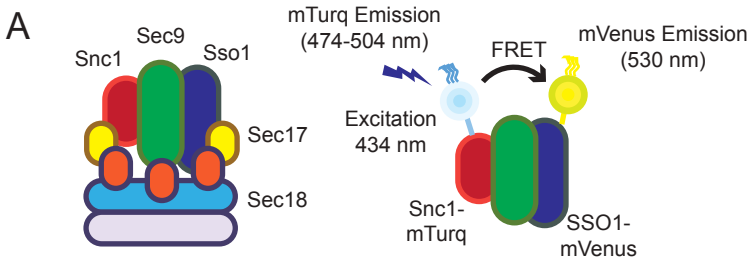
A
Snc1
Sec9
Sso1
Sec17
Sec18
mTurq Emission
(474-504 nm)
FRET
mVenus Emission
(530 nm)
Excitation
434 nm
Snc1-
mTurq
SSO1-
mVenus

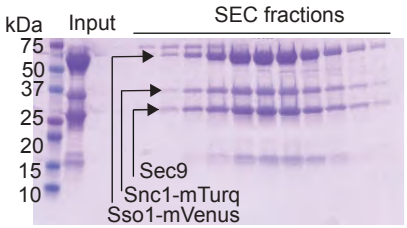
B
kDa
Input
SEC fractions
75
50
37
25
20
15
10
Sec9
Snc1-mTurq
Sso1-mVenus

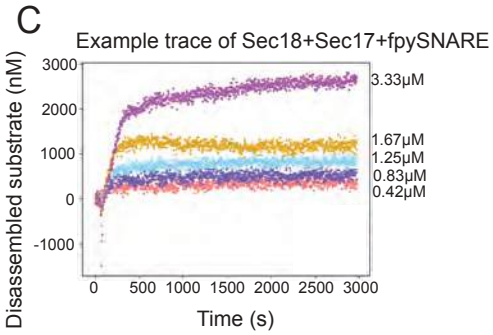
C
Example trace of Sec18+Sec17+fpySNARE
Disassembled substrate (nM)
3000
2000
1000
0
-1000
3.33μM
1.67μM
1.25μM
0.83μM
0.42μM
0
500
1000
1500
2000
2500
3000
Time (s)

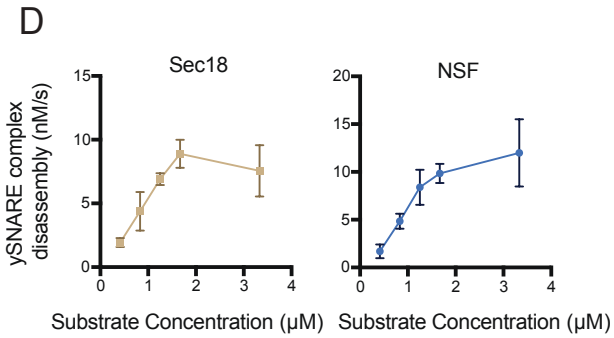
D
Sec18
NSF
ySNARE complex
disassembly (nM/s)
Substrate Concentration (μM)
Substrate Concentration (μM)

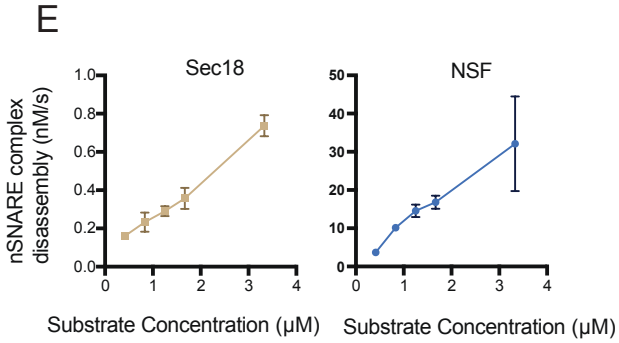
E
Sec18
NSF
nSNARE complex
disassembly (nM/s)
Substrate Concentration (μM)
Substrate Concentration (μM)

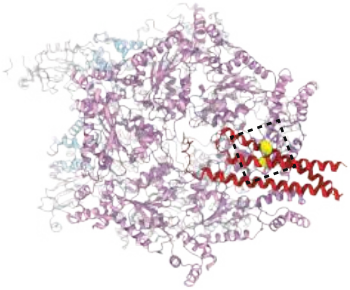
F

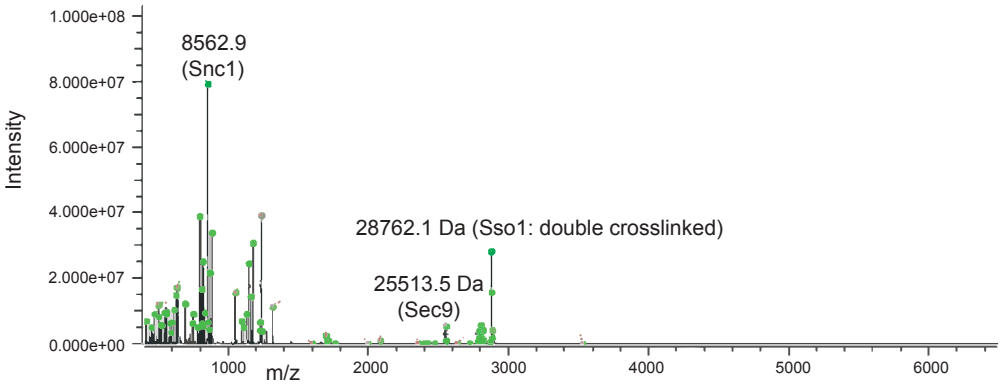
G
8562.9
(Snc1)
28762.1 Da (Sso1: double crosslinked)
25513.5 Da
(Sec9)
Intensity
m/z

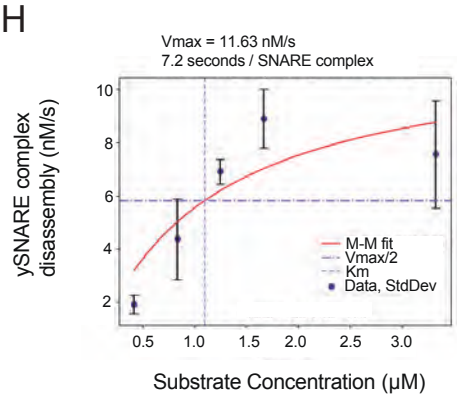
H
Vmax = 11.63 nM/s
7.2 seconds / SNARE complex
ySNARE complex
disassembly (nM/s)
M-M fit
Vmax/2
Km
Data, StdDev
Substrate Concentration (μM)

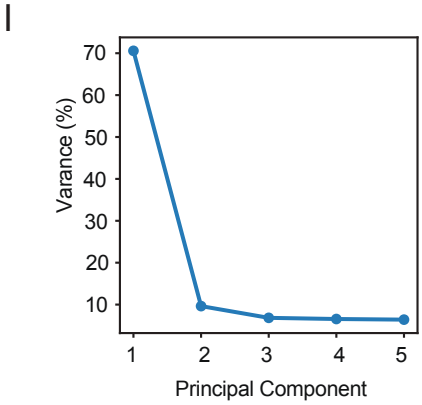
I
Varance (%)
Principal Component

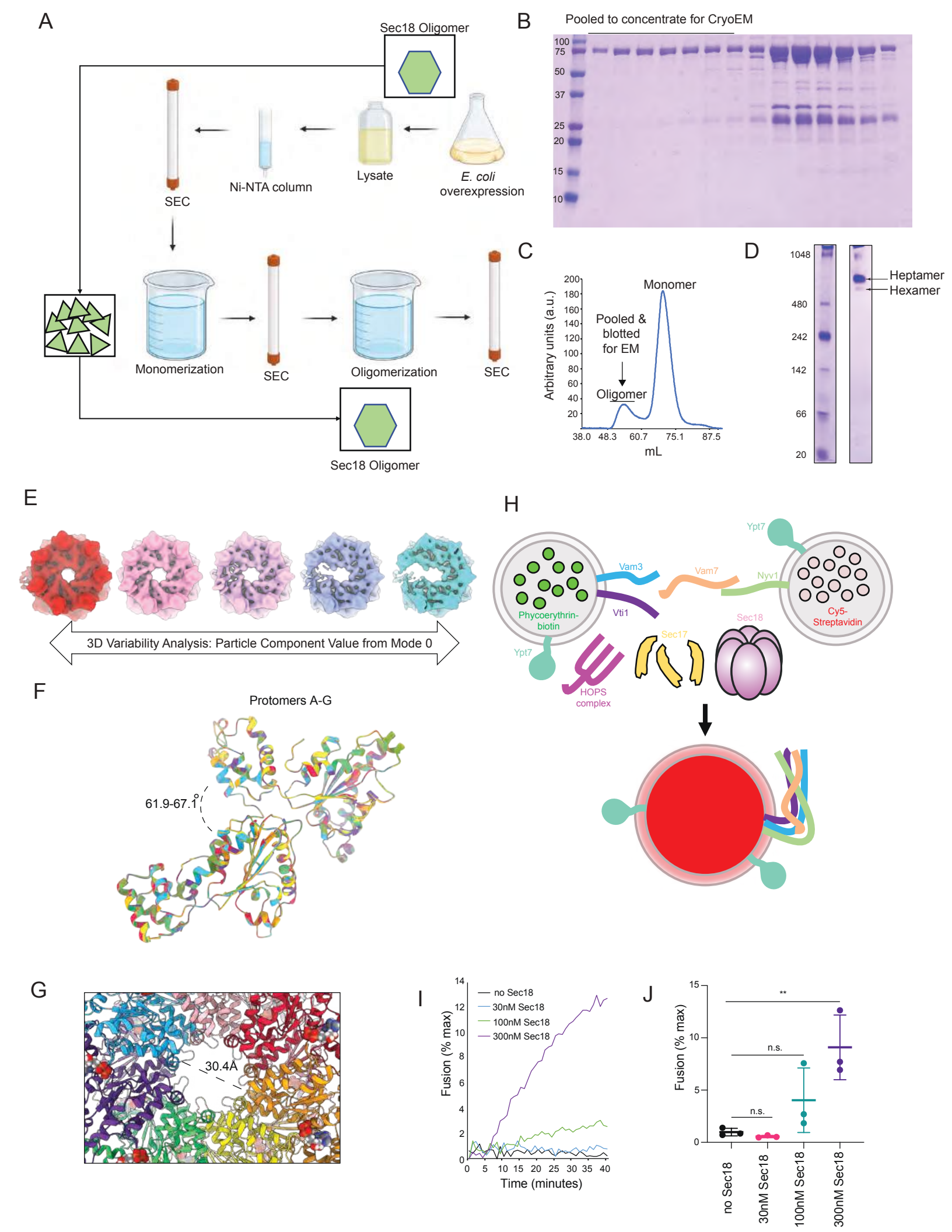
A
Sec18 Oligomer
SEC
Ni-NTA column
Lysate
E. coli overexpression
Monomerization
SEC
Oligomerization
SEC
Sec18 Oligomer
B
Pooled to concentrate for CryoEM
100
75
50
37
25
20
15
10
C
Monomer
Pooled & blotted for EM
Oligomer
Arbitrary units (a.u.)
mL
D
1048
480
242
142
66
20
Heptamer
Hexamer
E
3D Variability Analysis: Particle Component Value from Mode 0
F
Protomers A-G
61.9-67.1°
G
30.4Å
H
Ypt7
Vam3
Vam7
Nyv1
Vti1
Phycoerythrin-biotin
Cy5-Streptavidin
Sec18
Sec17
Ypt7
HOPS complex
I
no Sec18
30nM Sec18
100nM Sec18
300nM Sec18
Fusion (% max)
Time (minutes)
J
Fusion (% max)
**
n.s.
n.s.
no Sec18
30nM Sec18
100nM Sec18
300nM Sec18

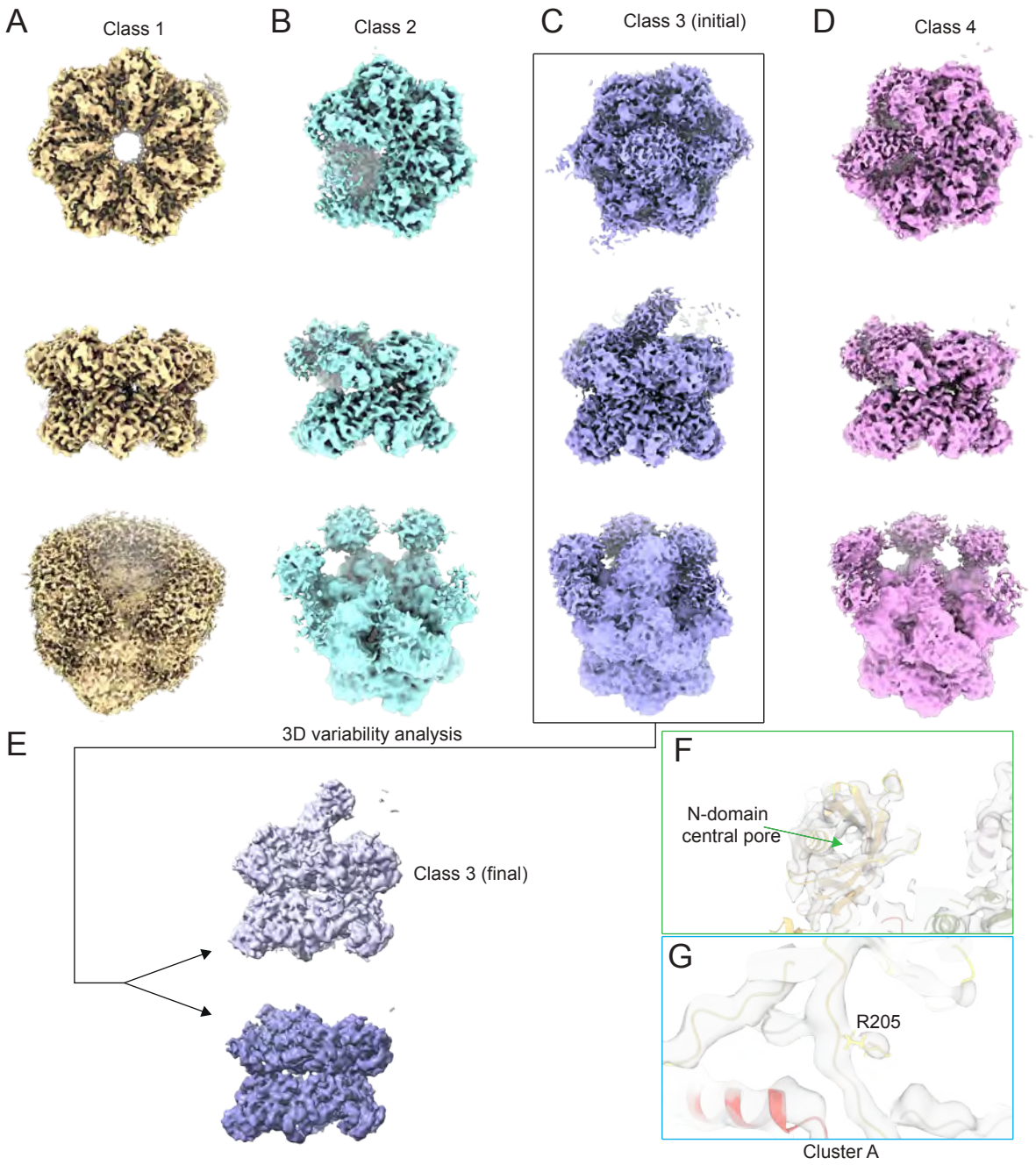
A
Class 1
B
Class 2
C
Class 3 (initial)
D
Class 4
E
3D variability analysis
Class 3 (final)
F
N-domain
central pore
G
R205
Cluster A

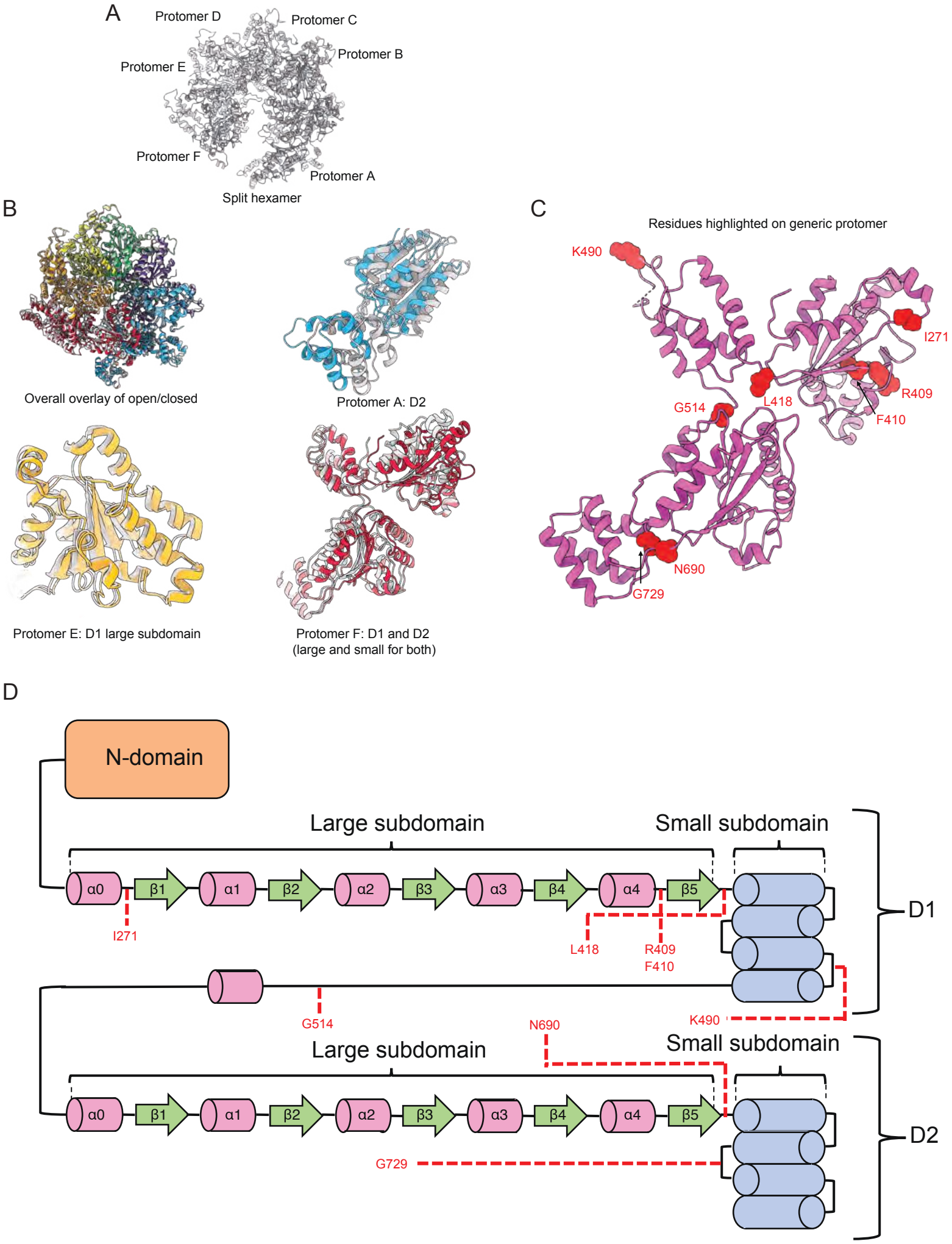
A
Protomer D
Protomer C
Protomer B
Protomer E
Protomer F
Protomer A
Split hexamer
B
Overall overlay of open/closed
Protomer A: D2
Protomer E: D1 large subdomain
Protomer F: D1 and D2
(large and small for both)
C
Residues highlighted on generic protomer
K490
I271
R409
L418
G514
F410
N690
G729
D
N-domain
Large subdomain
Small subdomain
α0
β1
α1
β2
α2
β3
α3
β4
α4
β5
D1
I271
L418
R409
F410
G514
K490
N690
Large subdomain
Small subdomain
α0
β1
α1
β2
α2
β3
α3
β4
α4
β5
D2
G729

Supplementary Information

Sec18 side-loading is essential for universal SNARE recycling across cellular contexts

Yousuf A. Khan[1,2,3,4,9], K. Ian White[1,2,3,4,5], Richard A. Pfuetzner[1,2,3,4,5], Bharti Singal[6],

Luis Esquivies[1,2,3,4,5], Garvey Mckenzie[7], Fang Liu[7], Katherine DeLong[1],

Ucheor B. Choi[1,2,3,4,5], Elizabeth Montabana[6], Theresa Mclaughlin[7], William T. Wickner[8],

Axel T. Brunger[1,2,3,4,5,9]

[1]Department of Molecular and Cellular Physiology, Stanford University, Stanford, CA, USA
[2]Department of Neurology and Neurological Sciences, Stanford University, Stanford, CA, USA
[3]Department of Structural Biology, Stanford University, Stanford, CA, USA
[4]Department of Photon Science, Stanford University, Stanford, CA, USA
[5]Howard Hughes Medical Institute, Stanford University, Stanford, CA, USA
[6]Stanford Cryo-EM microscopy center, Stanford University, Palo Alto, CA, USA
[7]Stanford University Mass Spectrometry, Stanford University, Palo Alto, CA, USA
[8]Department of Biochemistry and Cell Biology, Geisel School of Medicine at Dartmouth, Dartmouth College, Hanover, NH 03755.
[9]Correspondence: yousuf@stanford.edu (YAK), brunger@stanford.edu (ATB)

Table of Contents

Supplementary Information 1
Table of Contents 2
Supplementary discussion 3
Supplementary discussion references 5
Supplementary Figure Legends 6
Supplementary Figure 1 7
Supplementary Figure 2 8
Supplementary Figure 3 9
Supplementary Figure 4 10
Supplementary Figure 5 11
Supplementary Figure 6 12
Supplementary Figure 7 13
Supplementary Figure 8 14

Supplementary discussion

Cross complementation experiments

In our cross-complementation experiments, Sec18 and Sec17 disassembled neuronal and yeast SNARE complexes (**Extended Data Figure 5D-E**), like NSF and α-SNAP disassembling ySNARE. NSF disassembled the ySNARE complex at a rate comparable to Sec18 (**Extended Data Figure 5D**), but, interestingly, Sec18 disassembled neuronal SNARE slower than NSF, ~50-fold slower (**Extended Data Figure 5E**). This cross-complementation activity is corroborated by the high sequence and structural similarities between the yeast and neuronal systems. Despite differences in the SNARE substrate primary sequences, the substrate adopts a similar backbone conformation inside the pore of the D1 ATPase ring in both the yeast and neuronal systems (**Extended Data Figure 4C**).

Variability in N-domain engagement and Sec17 stoichiometry underlies substrate engagement

The eight classes from the non-hydrolyzing y20S dataset also show differences in the ySNARE-Sec17-Sec18-N-domain subcomplex arrangement ("spire") and stoichiometry above the D1 ring of the y20S complex before disassembly (**Figure 2D-E**). Based on an unbiased Cα clustering algorithm (**Methods**), we found that the eight classes fall into four clusters. In cluster 1, classes 1 and 2 with two Sec17 adaptor molecules (the density for the third adaptor is weak) are bound by only three N-domains. In cluster 2, classes 3-5 with a stable, U-shaped formation of three Sec17 molecules are bound by 3 or 4 N-domains. Cluster 3 is defined by a more stable arrangement of the U-shaped Sec17 arrangement again but with an N-domain contacting at least one Sec17 adaptor protein. Lastly, in cluster 4, Y20S class 8 has all five proximal protomers' N-domains engaging the Sec17 adaptor proteins.

Comparing the most extreme class averages in this dataset (class 1 and class 8, **Figure 2D**), the two Sec17 molecules lack the surface area to fully cover the exposed SNARE surface, which is covered upon binding a third Sec17 molecule (note that the linker between the two Sec9 SNAREs prevents a fourth Sec17 molecule from binding). This configuration also leads to a difference in the angle of the spire relative to the ring, where class 1's spire has an acute angle relative to the D1 ring. In contrast, class 8's spire is almost perpendicular. α-SNAP initially binds the SNARE complex with a 1:1 stoichiometry[7], yet structural and single-molecule FRET data shows that the 20S can form with up to 4 α-SNAP molecules[8–11]. Forming a 1:1 complex of SNARE and adaptor allows for Sec18/NSF recognition via N-domain engagement. Then, additional Sec17 molecules bind to the spire before disassembly, allowing for additional connection points between Sec18 and the spire. Regardless of class, the arrangement of the protomers around the SNARE substrate in the D1 ring and the D2 ring arrangement is nearly identical, as the longer N-D1 linker is flexible enough to accommodate a variety of N-domain configurations.

As in the case of α-SNAP, Sec17 interacts with the SNARE domain primarily through electrostatic interactions, consistent with structures of the neuronal 20S complex[8]. Alternating belts of electrostatic surface potentials complement each other in binding Sec17 adaptor proteins to the SNARE ternary complex (**Extended Data Figure 3B**). This observation may

explain how Sec18 and Sec17 can process many SNARE complexes composed of different primary sequences. The N-domains and Sec17p domains have complementary electrostatic surface potentials, suggesting that charge-charge interactions play a role in this interaction. The N-domains form cavities of opposite charge that complement the C-terminal portion of Sec17 upon binding (**Extended Data Figure 3C**).

Vacuolar SNARE fusion assay

Vacuolar SNARE components were also found in our *in vivo* crosslinking experiment (**Figure 1B**), making the vacuolar an attractive candidate for a functional test. The vacuolar proteoliposome fusion assay mimics the homotypic fusion of lysosomes/vacuoles[12] in which membranes expressing sets of SNAREs on each membrane must be preprocessed by Sec18, Sec17 and then passed to the HOPS complex to allow for homotypic fusion to occur. Using our preparation of Sec18, we observed fusion activity, which increased commensurately with the increase in Sec18 concentration. This observation confirmed that vacuolar SNARE processing was occurring, allowing homotypic fusion.

Substrate-free NSF under hydrolyzing conditions reveals additional conformations.

We investigated whether NSF may also form these ring states under hydrolyzing conditions without an SNARE substrate. We purified NSF, exchanged it into a hydrolyzing buffer (*i.e.*, in the presence of Mg^{2+}), and determined cryo-EM structures. We found two primary oligomeric states, consistent with our Sec18 data, a flat heptameric (**Extended Data Figure 7A**) and a hexameric (**Extended Data Figure 7B-D**) state. These states of NSF are like the heptameric and split hexameric states of Sec18, with a flat D1 ring and ADP in all D1 protomers and ATP in all D2 protomers.

The D1 ring of hexameric NSF contains density in the pore (**Extended Data Figure 7B–E**); the most likely interpretation of this density is that NSF is engaged with part of the N-domain from one of the protomers (**Extended Data Figure 7F–G**). This structure suggests that Sec18/NSF tends to fill the side-loading gap in the absence of a SNARE substrate. Taken together, either Sec18/NSF accepts an extra protomer that can easily slide in or out (or binds to its N-domain), or it accepts a SNARE substrate, leading to hexameric 20S or Y20S complex formation. We note that we did not observe a pronounced coordinated ring opening in this condition, although starting from the assembled 20S complex, we did observe a coordinated split-open state of both D1 and D2 rings[18] . Instead, the particular conditions of the substrate-free NSF sample shift it to a self-inhibited hexameric state where the N-terminal domain is engaged with the D1 pore.

Our observations of heptameric or auto-engaged hexameric complexes, also seen in other AAA+ proteins[1,2], follow a broader trend of inactive AAA+ conformations[3–6] that appear reversible in the presence of substrate. We also note that the interaction between protomers differs depending on their oligomeric state (**Supplementary Figure 7**).

Whether or not Sec18/NSF heptamers are present in the cell at physiologically relevant conditions is unclear and will be subject to future investigations.

Supplementary discussion references

1. Shen, P. S. Rearranging AAA+ architecture to accommodate folded substrates. *Nat. Struct. Mol. Biol.* **27**, 225–226 (2020).
2. Schumacher, J., Joly, N., Rappas, M., Zhang, X. & Buck, M. Structures and organisation of AAA+ enhancer binding proteins in transcriptional activation. *J. Struct. Biol.* **156**, 190–199 (2006).
3. Gaubitz, C. *et al.* Cryo-EM structures reveal high-resolution mechanism of a DNA polymerase sliding clamp loader. *eLife* **11**, e74175 (2022).
4. Shin, M. *et al.* Structural basis for distinct operational modes and protease activation in AAA+ protease Lon. *Sci. Adv.* **6**, eaba8404 (2020).
5. Gao, H. *et al.* Cryo-EM structures of human p97 double hexamer capture potentiated ATPase-competent state. *Cell Discov.* **8**, 1–13 (2022).
6. Cho, C. *et al.* Structural basis of nucleosome assembly by the Abo1 AAA+ ATPase histone chaperone. *Nat. Commun.* **10**, 5764 (2019).
7. Vivona, S. *et al.* Disassembly of All SNARE Complexes by N-Ethylmaleimide-sensitive Factor (NSF) Is Initiated by a Conserved 1:1 Interaction between α-Soluble NSF Attachment Protein (SNAP) and SNARE Complex*,. *J. Biol. Chem.* **288**, 24984–24991 (2013).
8. White, K. I., Zhao, M., Choi, U. B., Pfuetzner, R. A. & Brunger, A. T. Structural principles of SNARE complex recognition by the AAA+ protein NSF. *eLife* **7**, e38888 (2018).
9. Zhao, M. *et al.* Mechanistic insights into the recycling machine of the SNARE complex. *Nature* **518**, 61–67 (2015).
10. White, K. I. *et al.* NSF converts syntaxin clusters to a priming-ready state. *Unpublished*.
11. Kim, C. *et al.* Extreme parsimony in ATP consumption by 20S complexes in the global disassembly of single SNARE complexes. *Nat. Commun.* **12**, 3206 (2021).
12. Wickner, W. Membrane fusion: five lipids, four SNAREs, three chaperones, two nucleotides, and a Rab, all dancing in a ring on yeast vacuoles. *Annu. Rev. Cell Dev. Biol.* **26**, 115–136 (2010).
13. DAmico, K. A. *et al.* Structure of a membrane tethering complex incorporating multiple SNAREs. *Nat. Struct. Mol. Biol.* 1–9 (2024) doi:10.1038/s41594-023-01164-8.
14. Shvarev, D. *et al.* Structure of the HOPS tethering complex, a lysosomal membrane fusion machinery. *eLife* **11**, e80901 (2022).
15. Song, H., Orr, A. S., Lee, M., Harner, M. E. & Wickner, W. T. HOPS recognizes each SNARE, assembling ternary trans-complexes for rapid fusion upon engagement with the 4th SNARE. *eLife* **9**, e53559 (2020).
16. Song, H., Torng, T. L., Orr, A. S., Brunger, A. T. & Wickner, W. T. Sec17/Sec18 can support membrane fusion without help from completion of SNARE zippering. *eLife* https://elifesciences.org/articles/67578 (2021) doi:10.7554/eLife.67578.
17. Orr, A. & Wickner, W. Sec18 supports membrane fusion by promoting Sec17 membrane association. *Mol. Biol. Cell* **33**, ar127 (2022).
18. White, K. I. *et al.* NSF converts syntaxin clusters to a priming-ready state. *Unpublished*.

Supplementary Figure Legends

Supplementary Figure 1 | Gene ontology network of enriched processes based on enriched proteins in Sec18 coIP.

Supplementary Figure 2 | Processing information for the cryo-EM datasets. a) The general processing workflow that was employed for each dataset. b) Sec18 substratefree representative micrograph, Class2D, Class3D images, and final refinement depictions. c) Y20S EDTA representative micrograph, Class2D, Class3D images, and final refinement depictions. d) Y20S hydrolyzing condition representative micrograph, Class2D, Class3D images, and final refinement depictions. e) NSF hydrolyzing condition representative micrograph, Class2D, Class3D images, and final refinement depictions.

Supplementary Figure 3 | Distribution of particle orientation, FSC curves, and local resolution for all Y20S EDTA classes.

Supplementary Figure 4 | Distribution of particle orientation, FSC curves, and local resolution for all Y20S hydrolyzing classes.

Supplementary Figure 5 | Distribution of particle orientation, FSC curves, and local resolution for all Sec18 hydrolyzing classes.

Supplementary Figure 6 | Distribution of particle orientation, FSC curves, and local resolution for all NSF hydrolyzing classes.

Supplementary Figure 7 | Interprotomer interface comparison of substrate-engaged (top) and substrate-free (bottom) protomers of Sec18. Interacting residues at the interface are shown.

Supplementary Figure 8 | Full gel image of native gel of Sec18 hydrolyzing no substrate cryoEM sample, corresponding to cropped lanes shown in Extended Data Fig. 6d.

Supplementary Figure 1

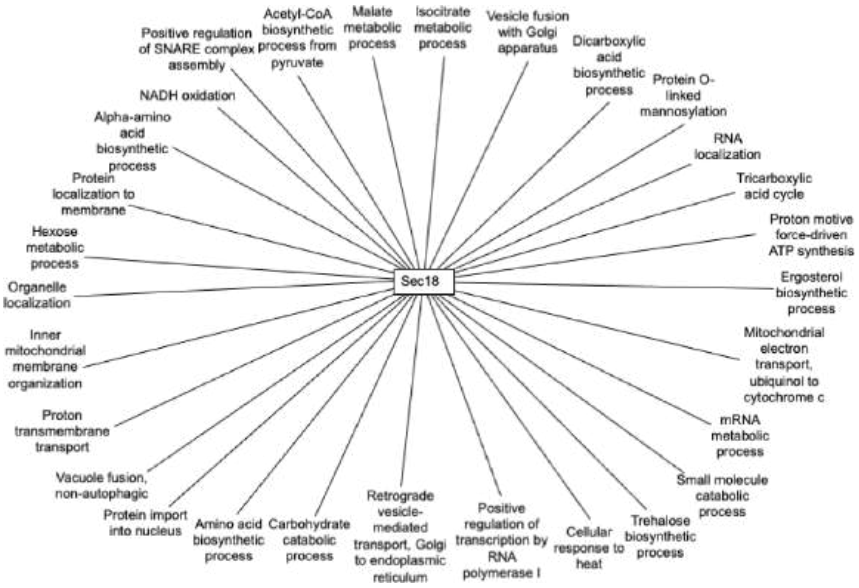

Supplementary Figure 2

A

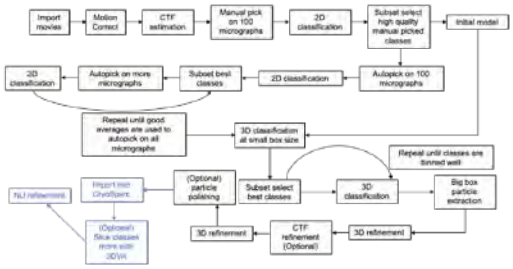

B

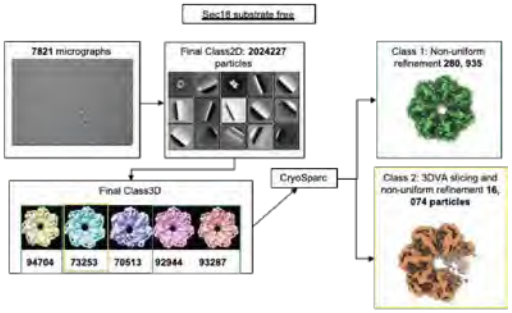

C

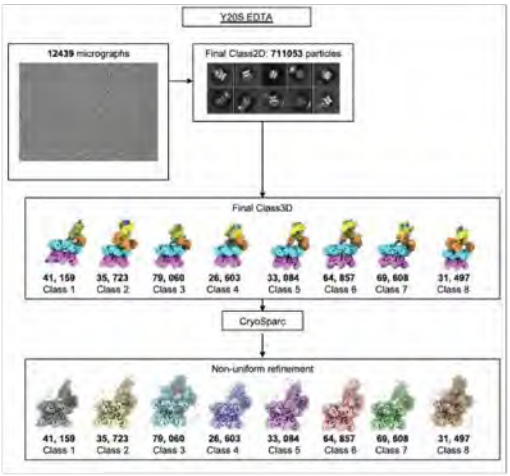

D

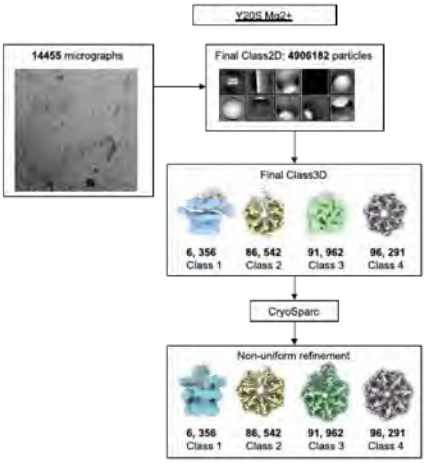

E

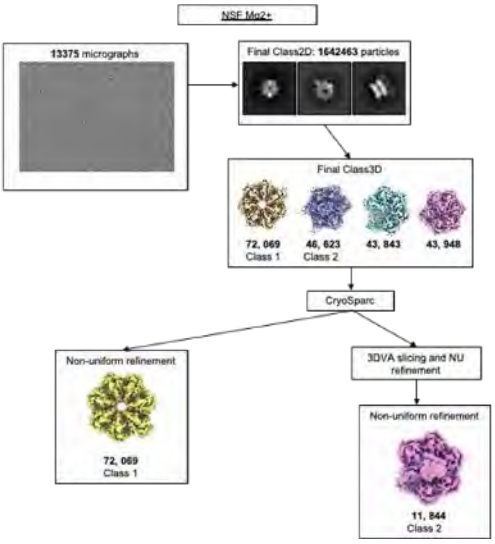

Supplementary Figure 3

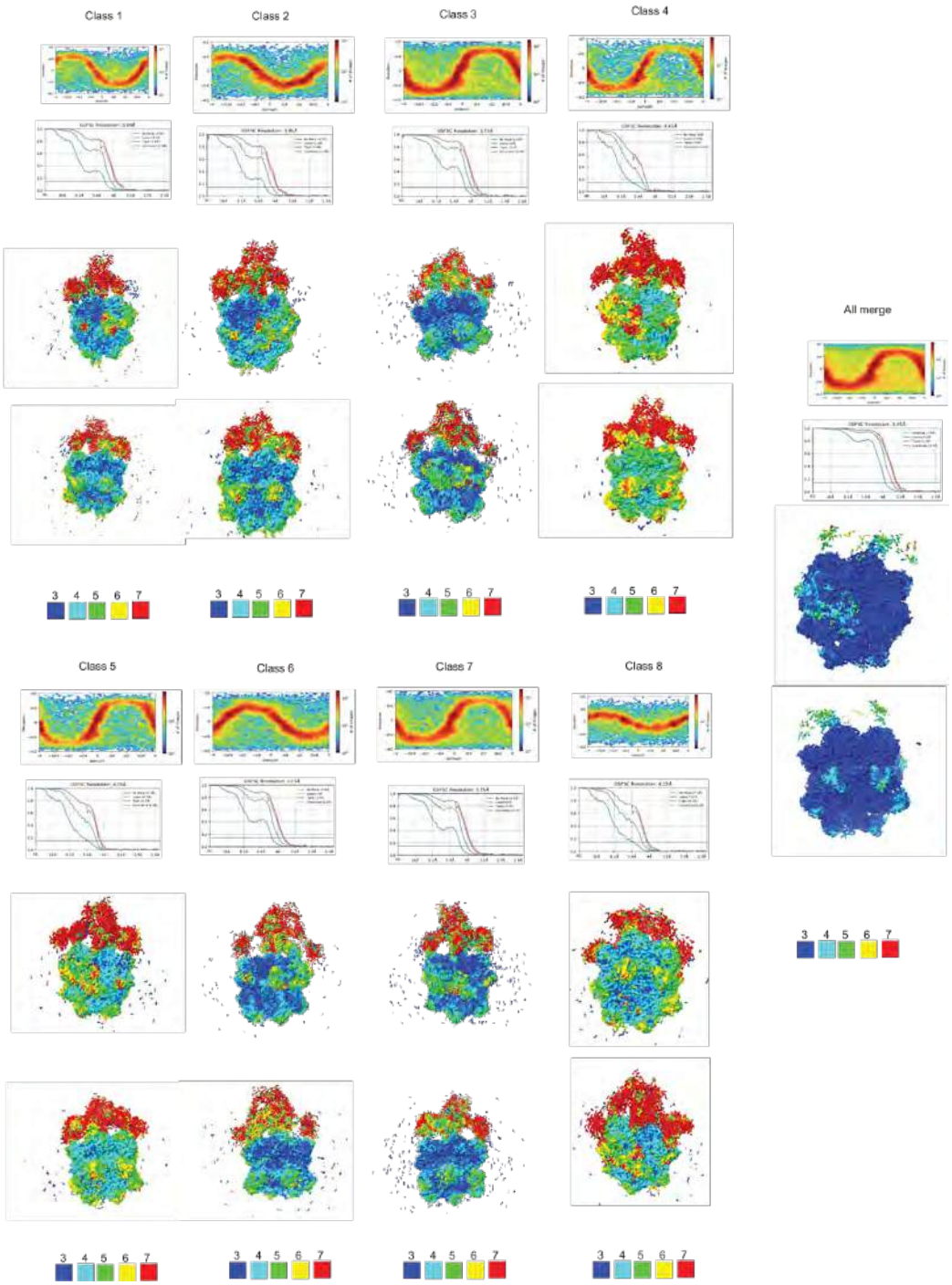

Supplementary Figure 4

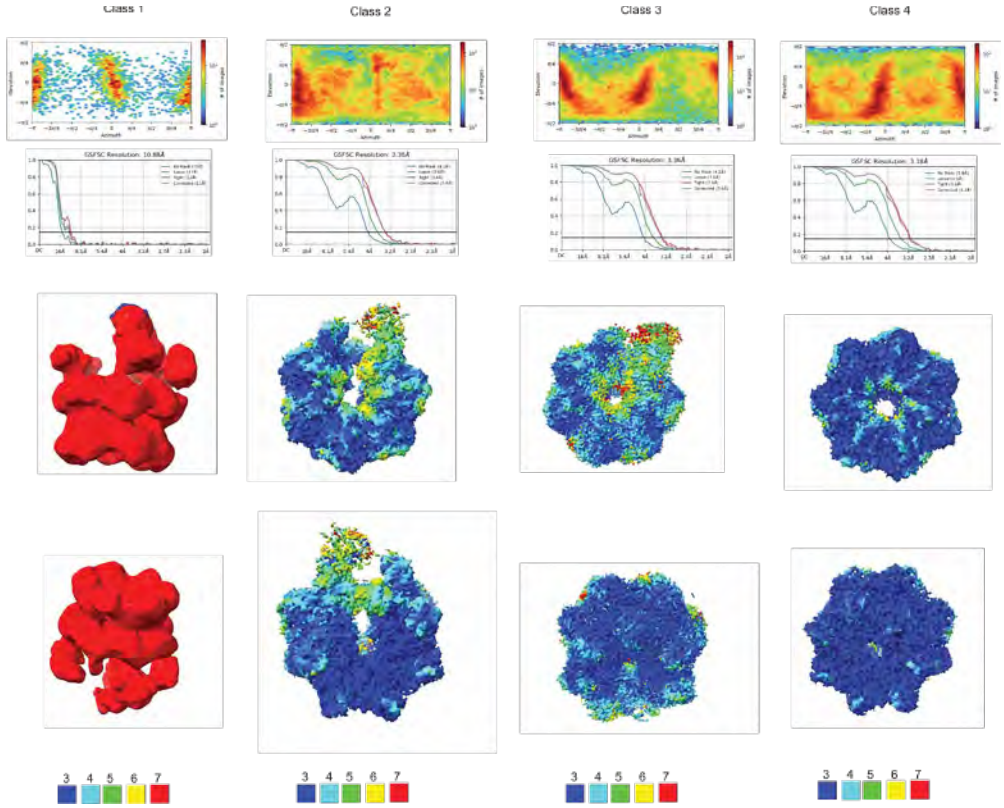

Supplementary Figure 5

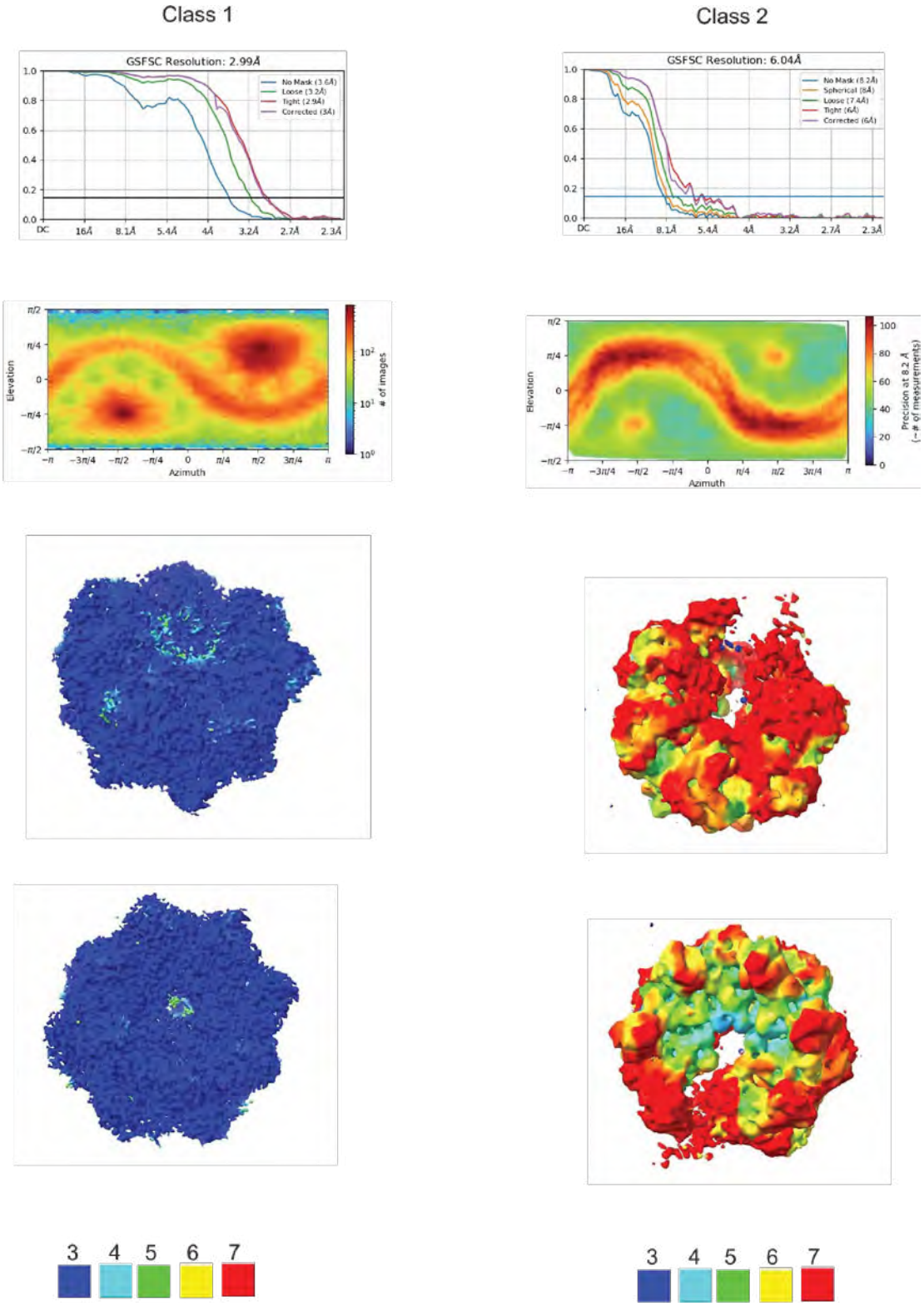

Supplementary Figure 6

Class 1

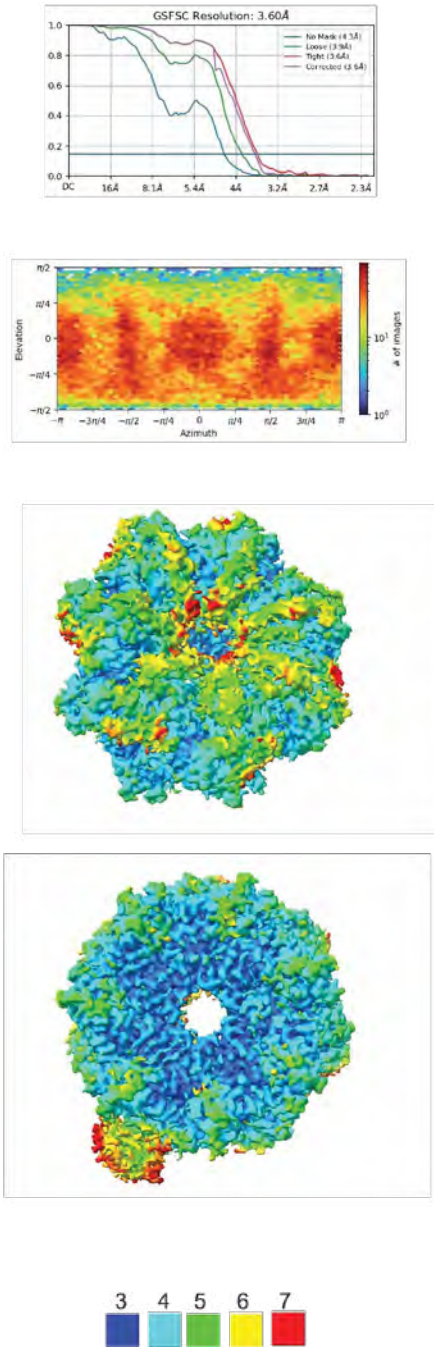

Class 2

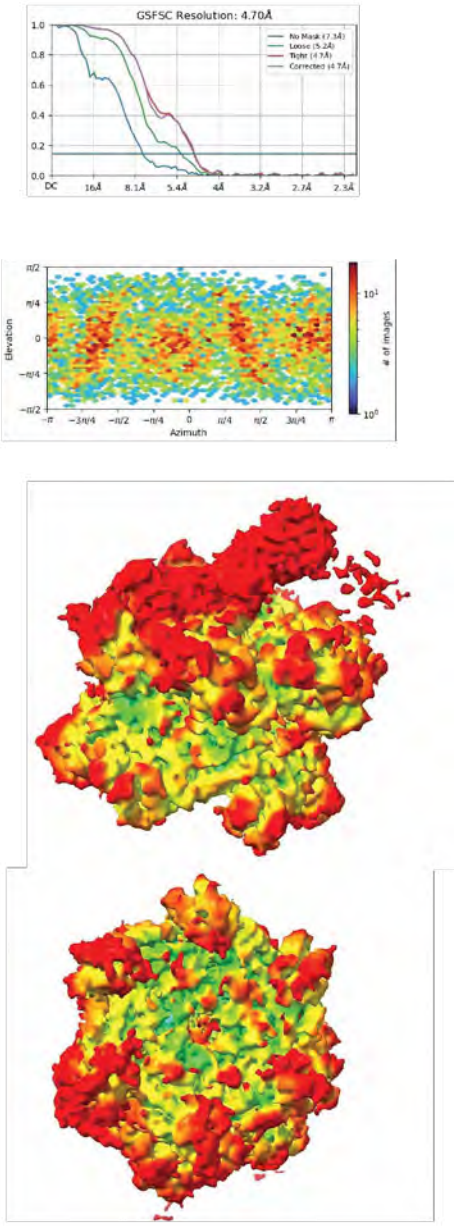

Supplementary Figure 7

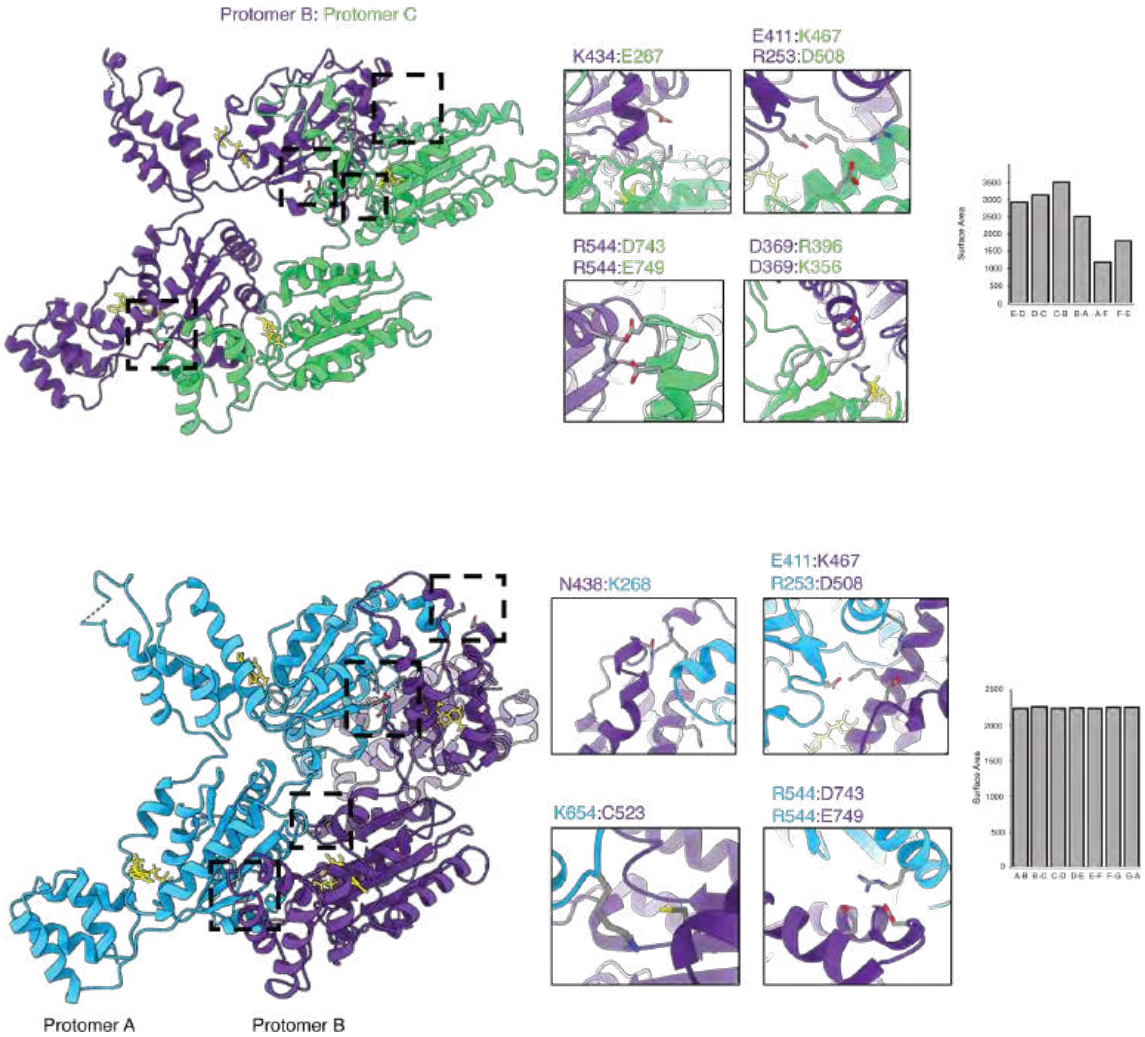

Supplementary Figure 8

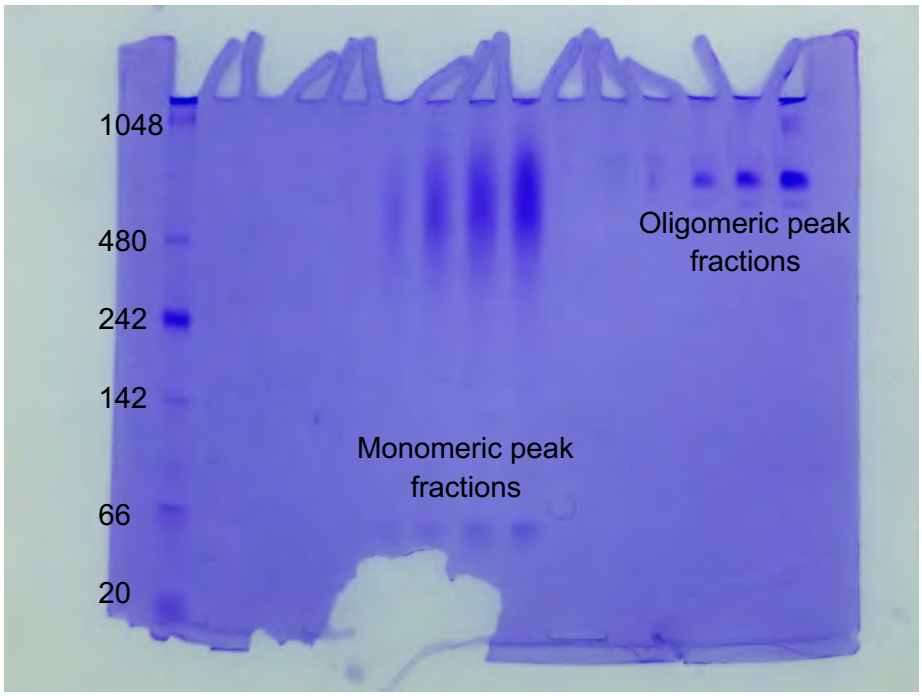

Extended Data Table 1 | Cryo-EM data collection, refinement, and validation statistics

	Y20S, non-hydrolyzing condition									Y20S, hydrolyzing condition				Sec18, hydrolyzing condition		NSF, hydrolyzing condition	
	#1 Class 1 (EMDB-45883) (PDB 9CRU)	#2 Class 2 (EMDB-48826) (PDB 9N22)	#3 Class 3 (EMDB-45885) (PDB 9CRX)	#4 Class 4 (EMDB-49380) (PDB PNG2)	#5 Class 5 (EMDB-49522) (PDB 9NLU)	#6 Class 6 (EMDB-49524) (PDB 9NLW)	#7 Class 7 (EMDB-49526) (PDB 9NLY)	#8 Class 8 (EMDB-49527) (PDB 9NLZ)	#9 All Merge D1/D2 (EMDB-49528) (PDB 9NM1)	#10 Class 1 (EMDB-70472 , no model deposited)	#11 Class 2 (EMDB-49801) (PDB 9NUD)	#12 Class 3 (EMDB-49802) (PDB 9NUE)	#13 Class 4 (EMDB-49824) (PDB 9NUZ)	#14 Class 1 (EMDB-49826 (PDB 9NV1)	#15 Class 2 (EMDB-49825) (PDB 9NV0)	#16 Class 1 (EMDB-49831) (PDB 9NV9)	#17 Class 2 (EMDB-49833) (PDB 9NVD)
Data collection and processing																	
Magnification	130,000×	130,000×	130,000×	130,000×	130,000×	130,000×	130,000×	130,000×	130,000x	130,000x	130,000x	130,000x	130,000x	130,000x	130,000x	130,000x	130,000x
Camera	Gatan K3	Gatan K3	Gatan K3	Gatan K3	Gatan K3	Gatan K3	Gatan K3	Gatan K3	Gatan K3	Falcon 4i	Falcon 4i	Falcon 4i	Falcon 4i	Gatan K3	Gatan K3	Gatan K3	Gatan K3
Voltage (kV)	300	300	300	300	300	300	300	300	300	300	300	300	300	300	300	300	300
Electron exposure (e–/Å2)	26.8	26.8	26.8	26.8	26.8	26.8	26.8	26.8	26.8	51.48	51.48	51.48	51.48	25.5	25.5	39.04	39.04
Defocus range (μm)	-1.0 to -2.0	-1.0 to -2.0	-1.0 to -2.0	-1.0 to -2.0	-1.0 to -2.0	-1.0 to -2.0	-1.0 to -2.0	-1.0 to -2.0	-1.0 to -2.0	-1.0 to -2.0	-1.0 to -2.0	-1.0 to -2.0	-1.0 to -2.0	-1.0 to -2.0	-1.0 to -2.0	-1.0 to -2.0	-1.0 to -2.0
Pixel size (Å, super-res)	0.548	0.548	0.548	0.548	0.548	0.548	0.548	0.548	0.548	0.49	0.49	0.49	0.49	0.548	0.548	0.548	0.548
Exposure time (seconds)	4	4	4	4	4	4	4	4	4	6.93	6.93	6.93	6.93	4	4	4	4
Number of frames per exposure	80	80	80	80	80	80	80	80	80	2133 (EER fractionation of 42)	2133 (EER fractionation of 42)	2133 (EER fractionation of 42)	2133 (EER fractionation of 42)	80	80	80	80
Number of movies	12,439	12,439	12,439	12,439	12,439	12,439	12,439	12,439	12,439	14455	14455	14455	14455	7821	7821	13375	13375
Symmetry imposed	C1	C1	C1	C1	C1	C1	C1	C1	C1	C1	C1	C1	C1	C1	C1	C1	C1
Final particle images (no.)	41,159	35,723	79,060	26,603	33,084	64,857	69,608	31,497	381,591	6,356	86,542	91,962	96,291	280,935	5,755	72,069	11,844
Global map resolution (Å)	3.89	3.91	3.73	4.61	4.29	3.73	3.75	4.13	3.4	10.88	3.38	3.36	3.18	2.99	7.83	3.60	4.70
Global map resolution range (Å): See supplementary information for resolution colored maps	3-7	3-7	3-7	3-7	3-7	3-7	3-7	3-7	2-4	9-12	2-6	2-7	2-4	2-3	4-8	3-6	4-7
FSC threshold	0.143	0.143	0.143	0.143	0.143	0.143	0.143	0.143	0.143	0.143	0.143	0.143	0.143	0.143	0.143	0.143	0.143
Model information																	

Initial model used (PDB code)	SNARE: 3B5N. Sec17: 1QQE/ AF-P32602-F1-v4. Sec18: AF-P18759-F1-v4	SNARE: 3B5N. Sec17: 1QQE/ AF-P32602-F1-v4. Sec18: AF-P18759-F1-v4	SNARE: 3B5N. Sec17: 1QQE/ AF-P32602-F1-v4. Sec18: AF-P18759-F1-v4	SNARE: 3B5N. Sec17: 1QQE/ AF-P32602-F1-v4. Sec18: AF-P18759-F1-v4	SNARE: 3B5N. Sec17: 1QQE/ AF-P32602-F1-v4. Sec18: AF-P18759-F1-v4	SNARE: 3B5N. Sec17: 1QQE/ AF-P32602-F1-v4. Sec18: AF-P18759-F1-v4	SNARE: 3B5N. Sec17: 1QQE/ AF-P32602-F1-v4. Sec18: AF-P18759-F1-v4	SNARE: 3B5N. Sec17: 1QQE/ AF-P32602-F1-v4. Sec18: AF-P18759-F1-v4	Sec18: AF-P18759-F1-v4	Y20S EDTA Class 1	*De novo*	*De novo*	*De novo*	*De novo*	*De novo*	3J94	3J94
Bond RMSD (Å)	0.008	0.006	0.007	0.005	0.006	0.005	0.006	0.005	0.006	No model deposited	0.005	0.004	0.004	0.004	0.005	0.005	0.006
Angle RMSD (°)	1.322	0.952	1.212	0.904	1.111	0.964	0.839	0.852	1.051	No model deposited	1.261	0.957	0.793	0.771	1.077	1.169	1.228
Molprobity score	1.64	1.48	1.59	1.45	1.17	1.47	1.16	1.24	1.56	No model deposited	1.25	1.22	1.74	1.42	1.13	1.49	1.08
Clashscore, all atoms	5.61	3.73	5.26	3.55	1.58	4.65	1.79	1.72	4.16	No model deposited	2.84	2.30	3.93	3.57	1.20	1.08	1.53
Ramachandran. Favored/Allowed/Disfacored (%)	95.17 4.55 0.28	95.48 4.46 0.06	95.52 4.21 0.27	95.59 4.13 0.28	96.05 3.77 0.18	96.42 3.44 0.14	96.51 3.40 0.08	96.12 3.63 0.24	94.81 5.03 0.16	No model deposited	96.95 2.92 0.14	96.68 3.32 0.00	95.19 4.52 0.29	96.03 3.97 0.00	95.79 4.11 0.10	95.81 4.19 0.00	97.34 2.14 0.52
Rotamer outliers (%)	0.51	0.30	0.12	0.12	0.89	0.60	0.57	1.17	0.66	No model deposited	0.08	0.00	1.96	0.93	0.79	3.25	1.20
Cβ outliers (%)	0.00	0.02	0.00	0.00	0.00	0.00	0.00	0.02	0.00	No model deposited	0.04	0.24	0.00	0.00	0.00	0.00	0.03
CaBLAM outliers (%)	2.38	2.11	2.29	2.41	2.05	1.93	2.01	2.00	3.07	No model deposited	0.93	1.63	1.22	0.99	0.93	1.35	1.27
Model resolution (0.5)	4.20	4.55	4.60	5.50	4.50	4.30	4.40	5.0	3.50	No model deposited	3.50	3.60	3.40	3.20	9.25	3.80	5.20